Joint Centre for Mesoscale Meteorology, Reading, UK

Contributions to the AMS/ RMS Conference on Mesoscale Processes Reading, 9-13 September 1996

Internal Report No. 63

June 1996

Met Office Joint Centre for Mesoscale Meteorology Department of Meteorology
University of Reading PO Box 243 Reading RG6 6BB United Kingdom
Tel: +44 (0)118 931 8425 Fax: +44 (0)118 931 8791
www.metoffice.com

Designed and produced by the Met Office © Crown copyright 2001 01/0240 The Met Office logo is a registered trademark.

CONTRIBUTIONS TO THE AMS/RMS CONFERENCE ON MESOSCALE PROCESSES

READING, 9-13 SEPT 1996

CONTENTS

1.1	PV advection and the omega equation	Brian Hoskins and Wyn Jones
3.2	Some questions regarding the dry intrusions associated with extratropical cyclones	Keith A Browning
3.3	Mesoscale dynamics associated with tropopause folds	Alan J Thorpe
4.5	Barotropic instability in a uniform strain	Douglas Parker
P5.6	Mesoscale structures in baroclinic life cycles	J Methven and B J Hoskins
P5.18	Variation of frontal and precipitation structure along a cold front	Keith A Browning and Nigel M Roberts
P5.27	Fronts 92 10P1 - Mesoscale structures associated with snow sublimation	S A Clough
P6A.1	3D radiative-convective equilibrium in the tropical atmosphere	A M Tompkins and G C Craig
P7A.17	Numerical experiments on the tropical cyclone eye	S L Gray and G C Craig
P7A.18	Evolution of tropical cyclone boundary layer	Chien-Liang Uang and Chris Thorncroft
P7B.3	Lee vortices due to flow past mesoscale mountains	Jorge Gutiérrez and Alan J Thorpe
P7B.14	Richardson number variation of stable boundary layer flow over hills	J J Holden, S E Belcher and S H Derbyshire
P7B.26	Omega-equation attribution applied to severe weather events in the western Mediterranean	Maria Athanassiadou and Alan J Thorpe
P12.8	Singular vector calculations for cases of cyclogenesis in the north Atlantic storm-track	Andrea Montani, Roberto Buizza and Alan J Thorpe

P12.12	A new PV-based method for short-range weather forecasting quality control and intervention	Meral Demirtas and Alan J Thorpe
14.1	Use of coincident aircraft and radar observations to verify and derive parametrization of cloud microphysics in mesoscale model forecast of frontal cloud	Anthony J Illingworth, Susan P Ballard, John W G Thomason and Virginia Marecal

PV ADVECTION AND THE OMEGA EQUATION

Brian Hoskins* and Wyn Jones

University of Reading
Reading, England

1. INTRODUCTION

One of the aims of this study is to tie together three different perspectives on mid-latitude synoptic systems: isentropic relative flow, omega equation and potential vorticity. The discussion will be given for an adiabatic system, with diabatic effects to be considered at a later stage.

1.1 Isentropic Relative Flow

The assumption is made that the system of interest is steady in a frame moving with the system speed, $\underset{\sim}{c}$. Therefore, in this coordinate system, the air moves along isentropic surfaces and w is equal to the isentropic upgliding value

$$w_{IU} = -\left[(\underset{\sim}{v} - \underset{\sim}{c}).\nabla\theta\right]/\frac{\partial\theta}{\partial z} . \quad (1)$$

It might be expected that this would be a reasonable first approximation if the time scale for system change is much smaller than the advective time-scale.

1.2 Omega Equation

The maintenance in time of a balance between the flow field and the thermodynamic state quite generally leads to a diagnostic equation. For quasi-geostrophic (QG) theory the maintenance of thermal wind balance leads to the omega equation. The forcing term for this elliptic equation for w is a function of the pressure field that can be written in a number of ways. The relationship between the approximate form (1) and the solution of the QG omega equation is not obvious. For a predictive system, the vorticity equation can be used to predict the pressure field, with the omega equation giving w.

1.3 Potential Vorticity (PV)

In the PV approach, the predictive equation is the conservation of PV (and boundary temperature) with a balance condition giving $\underset{\sim}{v}$, θ etc. The w-field is implicit in the theory. Hoskins et al (1995) describe how the vorticity changes imply that there must be ascent ahead of an upper PV maximum and descent behind it.

* *Corresponding author address:* Brian J Hoskins , University of Reading, Dept. of Meteorology, Reading RG6 2AU, UK; e-mail <hoskins@met.reading.ac.uk>

2. THE PV FORM OF THE OMEGA EQUATION

The link between these three approaches, all of which involve w implicitly or explicitly is given by the form of the QG omega equation given in the Appendix of Hoskins et al (1985). For any coordinate system speed, $\underset{\sim}{c}$, the QG w may be written:

$$w = w_{IU} + w_{PVA} + w_{BTA} . \quad (2)$$

Here, w_{IU} is the isentropic upglide defined in (1),
w_{PVA} the solution of an omega-type equation with forcing proportional to the vertical derivative of the coordinate system relative $QGPV$ advection with $w=0$ on horizontal boundaries,
and w_{BTA} is the solution of an omega-type equation with zero forcing but $w=-w_{IU}$ on horizontal boundaries i.e. proportional to boundary temperature advection.

Thus if $\underset{\sim}{c}$ is taken to be the system speed, $w_{PVA} + w_{BTA}$ is the departure from simple isentropic relative flow. Further it can be shown that (2) is mathematically equivalent to any of the forms of the omega equation. The form (2) clearly highlights the role of PV. Thus it provides a link between the three perspectives on mid-latitude synoptic systems.

3. APPLICATION TO THE EADY MODEL

The total vertical velocity for a neutral, lower boundary mode is shown in Fig. 1. There is ascent ahead of the trough and descent behind, there being no tilts in the vertical for this neutral mode. For the Eady model $QGPV$ and w_{PVA} are identically zero. For a coordinate system moving with the phase speed of the mode, here $\overline{u}$ (1.6km), w_{BTA} is also zero and $w = w_{IU}$. This must be the case for any neutral mode since the isentropes must be frozen in a coordinate system moving with the mode.

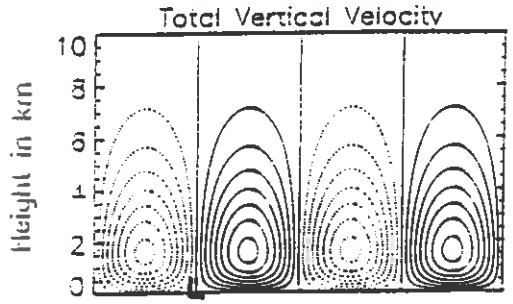

Figure 1. A longitude - height section of w in a 2-D Eady mode at a wavelength below the short wave cut-off. Contours at negative values are dashed . L marks the position of the surface low.

If, however, the coordinate system moves with the speed of the lower boundary flow, then w_{IU} and w_{BTA} have cancelling extrema at the lower boundary which are nearly three times the magnitude of the free atmosphere extrema in w.

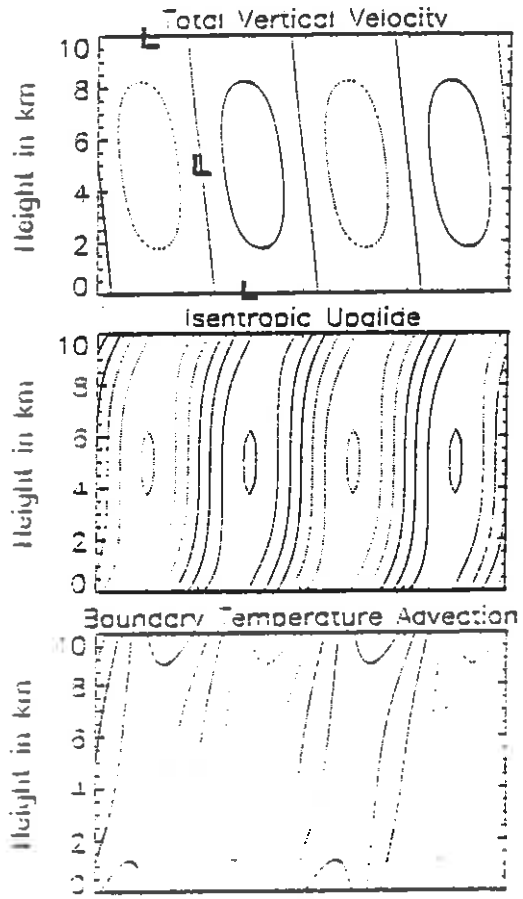

Figure 2. Longitude - height sections of w, and w_{IU} for the most unstable 2-D Eady mode. The co-ordinate system speed for w_{IU} and w_{BTA} is that of the mid-level flow. The contour interval is the same in the 3 plots.

Fig. 2 shows w for the most unstable Eady mode. It also shows w_{IU} and w_{BTA} for the mid-level flow, normal mode phase speed coordinate system.

The isentropic upglide component has the same flavour as for the neutral mode in Fig. 1. However at this longer zonal wavelength its vertical extent is such that its boundary magnitude is about $^2/_3$ of the mid-level magnitude.

Thus the cancellation with w_{BTA} is significant. At the mid-level ½ of w_{IU} is cancelled by w_{BTA} . This is in agreement with Eady's argument that the most unstable trajectory is at half the angle of the basic isentropes. If other speeds $\underset{\sim}{C}$ are used, the cancellation between w_{IU} and w_{BTA} is larger.

4. FURTHER COMMENTS.

Localised PV distributions, baroclinic wave life-cycles and real synoptic developments are also being considered using this analysis. Some ideas being explored are:

- the dominance of w_{IU} moving with the system speed,
- the role of w_{PVA} and w_{BTA} in giving the departure from neutral mode behaviour
- the determination of system speed by minimising the cancellations associated with, and the magnitudes of w_{PVA} and w_{BTA}.

5. REFERENCE

Hoskins, B.J., M.E. McIntyre and A.W. Robertson, 1985: On the use and significance of isentropic potential vorticity maps. Quart. J. Roy. Meteor. Soc., 111, 877-946.

SOME QUESTIONS REGARDING THE DRY INTRUSIONS (DIs) ASSOCIATED WITH EXTRATROPICAL CYCLONES

Keith A Browning*

Joint Centre for Mesoscale Meteorology, University of Reading
Reading, UK

1. INTRODUCTION

In satellite imagery, the signature of a developing cyclone undergoing frontal fracture (Shapiro and Keyser 1990) comprises a cloud head with extensive precipitation separated from a polar-front cloud-band (PFCB) by a dry slot (Fig 1) (Browning and Roberts 1994). An example can be seen in the IR image on the front cover of this volume. In some circumstances the dry slot may be much wider than shown in Fig 1. The dry slot marks the leading part of a re-ascending airflow that has recently descended from near tropopause level: this is the DI. Some of the DI air originates from the upper troposphere and some from the lower stratosphere (Wernli 1995). Ahead of bc in Fig 1 the DI overruns a shallow moist zone (SMZ) - see sounding in Fig 2 (from Browning et al 1995).

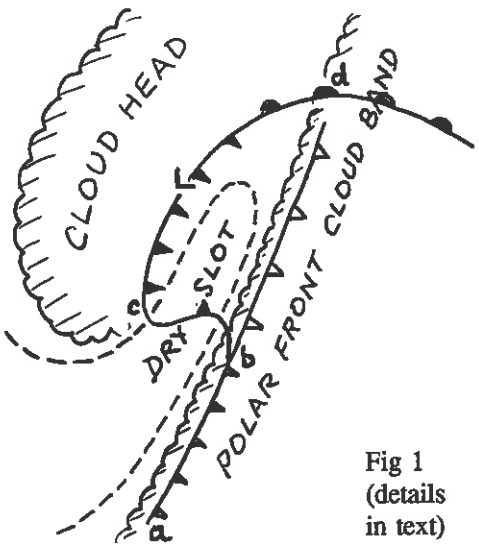

Fig 1 (details in text)

*Corresponding address: JCMM, Harry Pitt Building, Univ of Reading, Whiteknights Road, PO Box 240, Reading RG6 6FN, UK; e-mail <kabrowning@meto.govt.uk>. (The JCMM is supported by the Met Office and the Department of Meteorology, University of Reading).

The main fronts are marked on Fig 1. Along ab and cd, the cold fronts are sharp at the surface, often with line convection giving narrow cold frontal rainbands (see radar pictures on front cover). Along bc, where the DI overruns, the cold front is usually diffuse. Along bd, the right side of the DI is marked by an upper cold front. The fronts along bc and bd are better defined as θ_w-fronts than θ-fronts.

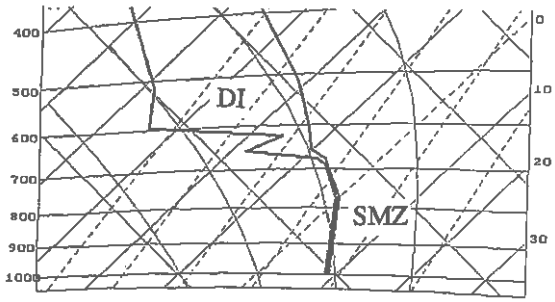

Fig 2

2. MULTIPLE STRUCTURE

DIs are seen as dark zones in water vapour (WV) imagery. They often have a multiple structure. Fig 3 (from Browning et al 1995) shows two such dark zones, with their respective surface

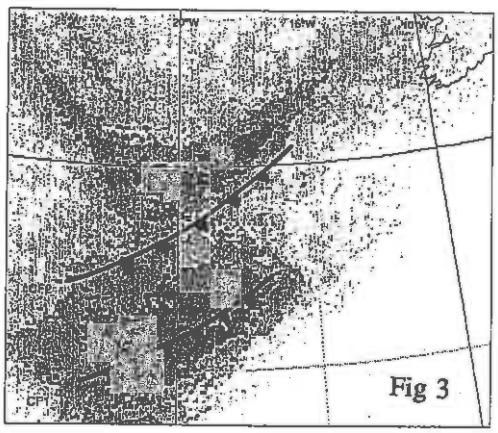

Fig 3

cold fronts. The latter often show up as lines of boundary-layer (BL) cloud, or rope clouds, just upwind of the dry-slot region (see visible image on front cover). These can develop and supersede the main cold front. Upon entering the dry-slot region they tend to evolve into upper cold fronts. WV imagery has poor resolution, especially in the vertical, and so it resolves only the more widely spaced cold pulses.

Sometimes a single DI, upon approaching the PFCB, is so strongly stretched that it subdivides, as shown by the 3-hourly sequence of WV dark zones in Fig 4. A mesoscale model run on this occasion (Browning and Golding 1995) showed that each DI gave rise to a mesoscale circulation, with its own dry slot and moist finger associated with a small cloud head (see Fig 5).

Fig 4

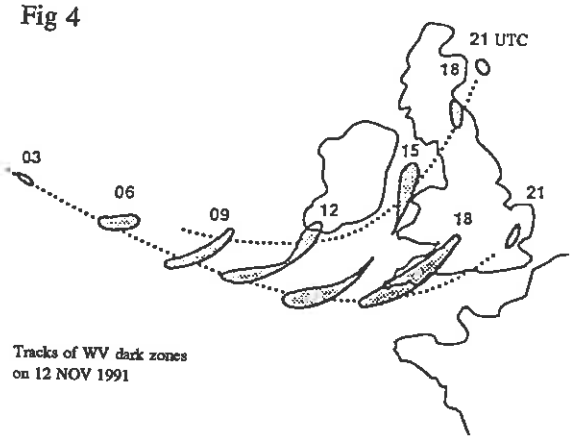

Tracks of WV dark zones on 12 NOV 1991

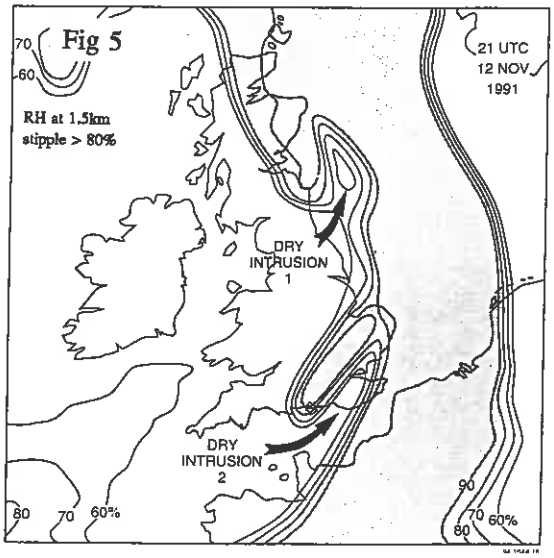

3. DIs & POTENTIAL VORTICITY

DIs are closely associated with high potential vorticity (PV) brought down within a tropopause fold (Reed 1955) - see cross section in Fig 6 (from Browning et al 1996). This tends to couple with diabatically-generated regions of high PV at low levels to produce rapid cyclogenesis (Hoskins et al 1985).

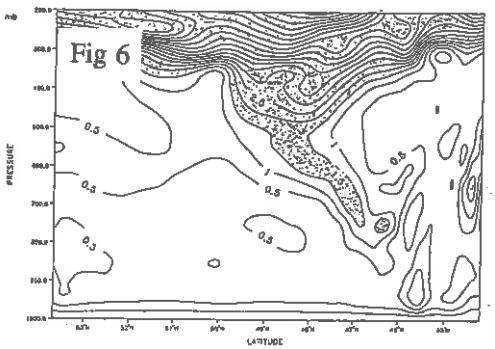

WV imagery can be used to validate and bogus model representations of upper-level PV forcing (Mansfield 1994). However, there is uncertainty as to which model-derived field is best for matching with the WV imagery in order to identify the early stages of folding. Fig 7(a) (adapted from Browning 1996) shows north-south (N-S) profiles through a tropopause fold and upper jet J (Fig 7(b). Curve 1 shows the darkness of the WV image. Corresponding model-derived profiles are: θ on PV=2pvu (curve 2a), height of PV=2pvu (curve 2b) and absolute vorticity, at 300mb say, (curve 3). Curves 2b and 3 both succeed in highlighting the dark zone as a 2-sided anomaly.

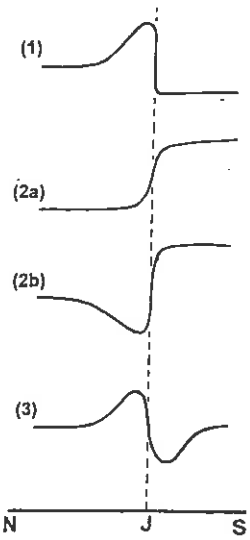

Fig 7(a)

Fig 7(b)

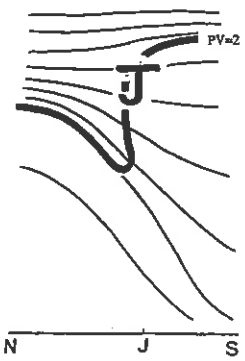

4. DIs & POTENTIAL INSTABILITY

Observations reveal that the descent of the tropopause fold, with its high PV, leads to differential rotation, with rotation decreasing downwards (Browning et al 1966). Fig 8, depicting a particular θ_w-surface at 950mb (solid curve) and 700mb (dashed) during rapid cyclogenesis, shows that the differential rotation leads to the development of an area of potential instability (PI) over the 6-h period between Figs 8(a) and (b). The area of PI (stippled in Fig 8(b)) is the dry-slot region. Air at and above 700mb in this region is in the overrunning DI; air below 700 mb is in the SMZ (see also Fig 2). Strongest PI and the most intense convection appear to occur when the DI and its associated high PV plunge down all the way to the BL (Browning and Golding 1995).

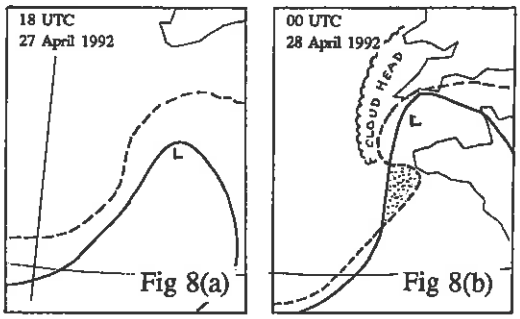

Fig 8(a) Fig 8(b)

5. FRONTAL TYPES

The pair of θ_w-isolines in Fig 8 indicate the slope of the θ_w-fronts. In the northern part of Fig 8(b) (corresponding to cd in Fig 1), where the dashed line extends to the west of the solid line, the front is an ana-front (see transverse circulation in bottom panel of Fig 9). This is the cloud-head region where moist BL air is extruded rearwards (stippled in Fig 9). An ana-front also occurs much farther south (ab in Fig 1). In between these two regions, in the stippled part of Fig 8(b), the front is a kata-front (top panel of Fig 9 showing a section along axis of dry slot). Detailed mesoanalysis (Browning 1995) shows that the circulation in parts of this region may be a hybrid between that of a pure kata- and ana-cold front (middle panel).

6. SOME QUESTIONS

Some questions to be resolved are: What determines whether the DI plunges all the way down to the BL? What diagnostics provide best

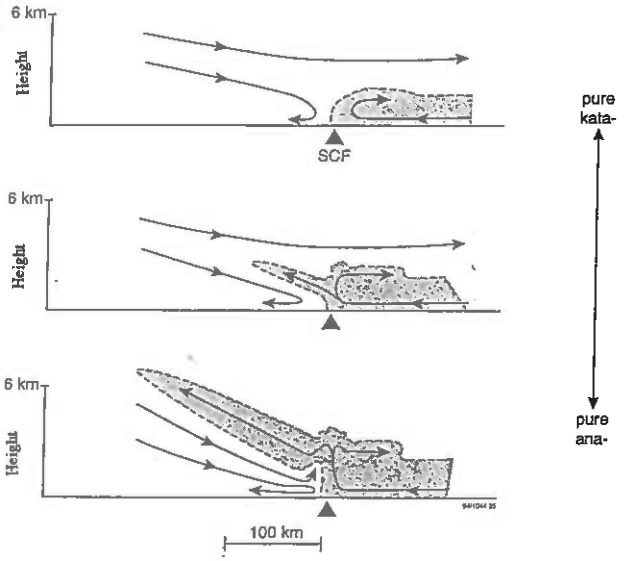

Fig 9

warning of a plunging DI? What determines the degree of differential rotation and production of PI? How universal is the relationship between a plunging DI and severe convective weather events? Does the scale of this process facilitate prediction of the smaller-scale convective events? How do DI substructures, and hence multiple cold fronts, develop? How do these cold fronts evolve from surface features to upper fronts and what BL processes are involved?

7. REFERENCES

Browning, K.A. and N.M.Roberts, 1994: *Quart.J.Roy.Meteor.Soc.*, **120**, 1535-1557.

Browning, K.A., 1995: *Tellus*, **47A**, 911-919.

Browning, K.A., S.A.Clough, C.S.A.Davitt, N.M.Roberts,T.D.Hewson and P.G.W.Healey 1995: *Quart.J.Roy.Meteor.Soc.*, **121**, 1229-1254.

Browning, K.A. and B.W.Golding, 1995: *Quart.J.Roy.Meteor.Soc.*, **121**, 463-493

Browning, K.A., 1996: *Meteor.Apps.*, **3**.

Browning, K.A., S.P.Ballard and C.S.A.Davitt 1996: *Mon.Wea.Rev.*, **124**.

Hoskins, B.J., M.E.McIntyre and A.W.Robertson 1985: *Quart.J.Roy.Meteor.Soc.*, **111**, 877-946

Mansfield, D., 1995: *Proc.Int.Symp, 1994 Bergen*, pp 326-331.

Reed, R.J., 1995: *J.Meteor.*, **12**, 226-237.

Shapiro, M.A. and D.Keyser 1990: Pp 167-191 in *Extratropical cyclones*. Am.Meteorol.Soc.

Wernli, R.J., 1995: PhD Thesis, ETH Zurich.

3.3 MESOSCALE DYNAMICS ASSOCIATED WITH TROPOPAUSE FOLDS

Alan J. Thorpe *

JCMM, University of Reading, UK

1. INTRODUCTION

Extreme undulations of the tropopause, sometimes involving tropopause folds, are commonplace in mature extratropical cyclones. It is tempting to attribute the onset of certain mesoscale phenomena, such as convection and vortices, to the descent of the tropopause to levels near the boundary layer; see observational evidence from Browning and Golding (1995) and Browning and Reynolds (1994). Tropopause folds are also important in cross-tropopause transport and probably in the dynamics of the cyclone itself; see Hirschberg and Fritsch (1991). In this paper the association between mesoscale features in the pattern of vertical motion and the presence of a tropopause fold is examined.

The semi-geostrophic (SG) theory in two dimensions is used as the basic tool for the analysis. Realistic solutions have been obtained by solving numerically the Sawyer-Eliassen cross-frontal circulation equation. Stretching and shearing deformation frontogenesis have rather distinctive patterns of vertical motion attributable to the fold. A key factor is that the fold is usually a mesoscale feature embedded in a larger-scale pattern of forcing. The relative positions of the fold and this forcing, the magnitude of the PV anomaly in the fold, and the horizontal extent of the fold together determine the mesoscale features of vertical motion attributable to the fold.

Another consequence of the tropopause funnel is that there is reduced static stability below the large PV contained in the funnel. It is important in considering the triggering of convection to ascertain whether there is a favourable colocation of the reduction in static stability due to the tropopause fold and the changes in the vertical motion pattern. Convective activity can be triggered by a lowered tropopause if this can occur. Additionally differential humidity advection caused by the fold may also have an important role in triggering convection but is not considered here.

* *Corresponding author address*: Alan J. Thorpe, Dept. of Meteorology, Univ. of Reading, Whiteknights, Reading RG6 6AU, UK; e-mail <A.J.Thorpe@reading.ac.uk>

2. RESUMÉ OF SEMI-GEOSTROPHIC EQUATIONS

The two-dimensional semi-geostrophic PV inversion equation transformed to geostrophic momentum (GM) coordinates, given by $X = x + v_g/f$ and $Z = z$, are:

$$PV = \frac{\frac{\partial^2 \Phi}{\partial Z^2}}{f^2 - \frac{\partial^2 \Phi}{\partial X^2}} \qquad (1)$$

where PV is the non-dimensional potential vorticity given by the expression: $PV = (\frac{g}{f^3 \theta_0}) \underline{\zeta}.\nabla\theta$, $\underline{\zeta}$ is the geostrophic vorticity, $\Phi = \phi + \frac{1}{2}({u_g}^2 + {v_g}^2)$ and ϕ is the geopotential.

The Sawyer-Eliassen cross-frontal circulation equation in these coordinates is:

$$\frac{\partial}{\partial X}\left(PV \frac{\partial \Psi}{\partial X}\right) + \frac{\partial^2 \Psi}{\partial Z^2} = \frac{2Q}{f^2} \qquad (2)$$

where $u = -\frac{\partial \Psi}{\partial Z}$ and $w = \frac{\zeta}{f} w^*$ and $w^* = \frac{\partial \Psi}{\partial X}$ are the ageostrophic wind components, Ψ is the ageostrophic flow streamfunction, and Q is the geostrophic forcing given in the transformed coordinates by:

$$Q = f\left(-\frac{\partial u_g}{\partial X}\frac{\partial v_g}{\partial Z} + \frac{\partial v_g}{\partial X}\frac{\partial u_g}{\partial Z}\right) \qquad (3)$$

3. ATTRIBUTION OF VERTICAL MOTION

There are 2 factors which contribute to the vertical motion. The first is the Q-vector forcing. This is in part determined by the existence of the PV anomaly contained in the fold as well as by the background PV distribution including that implied by the surface thermal pattern. The second is the role of the potential vorticity as a dielectric factor as it is a coefficient in the Sawyer-Eliassen equation (see Thorpe and Bishop 1995 for details concerning the electrostatic analogy). The

combination of these two effects can have a surprising outcome allowing the attribution of a pattern of vertical motion to the tropopause fold which includes, in different regions, a decrease **and an increase** in vertical motion.

To find the vertical motion attributable to the fold we calculate solutions of the Sawyer-Eliassen equation for a case with a deep undulation and a case with a shallow undulation of the tropopause. For brevity we shall refer to the difference between these two potential vorticity distributions as the PV fold anomaly; i.e. the potential vorticity distribution for the deep undulation is the sum of that for the shallow undulation and the fold anomaly. Other properties of the front, such as surface temperature pattern, are the same for the two cases. By taking the difference between the deep and shallow solutions we find that part of the vertical motion that is uniquely attributable to the PV fold anomaly.

To gain insight into this attribution methodology it is first convenient to manipulate the SG Sawyer-Eliassen equation. The streamfunction Ψ, in the deep undulation case, can be divided into a part, $\overline{\Psi}$, which is the solution of the equation for the shallow PV distribution and a (not necessarily small) contribution, Ψ', due to the presence of the PV fold anomaly. The equation for Ψ' is obtained by subtracting the equation for $\overline{\Psi}$ from the full equation (2) to give:

$$\frac{\partial}{\partial X}\left(PV\frac{\partial \Psi'}{\partial X}\right)+\frac{\partial^2\Psi'}{\partial Z^2}=-\frac{\partial}{\partial X}\left(PV'\overline{w}^*\right)+\frac{2Q'}{f^2} \tag{4}$$

where Q' is the incremental Q-forcing due to the fold anomaly, PV'. The first term on the right-hand-side of Equation (4) is an "ageostrophic" forcing as it depends on the vertical motion attributable to the shallow tropopause undulation as well as on the fold PV anomaly. It arises from that part of the dielectric factor acting due to the fold potential vorticity anomaly. Consequently the vertical motion due to the ageostrophic forcing, is such that: in the fold it is of the opposite sign, whilst adjacent to the fold, in the tropospheric air, it is of the same sign as the vertical motion attributable to the shallow tropopause undulation.

The change in the forcing Q' (the second term on the right-hand-side of Equation (4)) is a function of PV', which is in general a function of both $\overline{\Psi}$ and of Ψ'. This will be referred to as the additional "geostrophic" forcing as it depends on the geostrophic flow and temperature due to the fold PV anomaly.

4. RESULTS FOR THE TROPOPAUSE FUNNEL

Realistic, but idealised, tropopause structures have been used. The geostrophic flow is a consequence of the imposed boundary thermal pattern, which is kept fixed for the sake of clarity, and the internal PV structure which has been varied. These structures are assumed and have not arisen from a time integration from simpler initial conditions. Solutions of the circulation equation will be presented with various imposed Q forcings: stretching and shearing deformation and a combination of these two. These show that the contribution to the vertical motion attributable to the fold from the so-called geostrophic forcing is dominant but it is significantly modulated by the ageostrophic forcing. In these circumstances the vertical motion attributable to the fold is mostly due to differential potential vorticity advection. Hence, if there is frontogenesis then, there is ascent in the warm tropospheric air ahead of the fold and descent behind the fold which can be uniquely attributed to the fold PV anomaly.

These results indicate that tropopause folds can be associated with significant mesoscale structure in the vertical motion and static stability. In particular in the warm air ahead of the fold there is additional ascent which is sometimes accompanied by a reduction in the static stability due to the presence of the fold. This circumstance might be conducive to the stimulation of convection by a descending tropopause fold.

5. REFERENCES

Browning, K. A. and Golding, B. W. 1995 Mesoscale aspects of a dry intrusion within a vigorous cyclone. *Q. J. R. Meteorol. Soc.*, **121,** 463-493

Browning, K. A. and Reynolds, R. 1994 Diagnostic study of a narrow cold frontal rainband and severe winds associated with a stratospheric intrusion. *Q. J. R. Meteorol. Soc.*, **120,** 235-257

Hirschberg, P. A. and Fritsch, M. J. 1991 Tropopause undulations and the development of extra-tropical cyclones. Part II Diagnostic analysis and conceptual model. *Mon. Wea. Rev.*, **119,** 518-550

Thorpe, A. J. and Bishop, C. H. 1995 Potential vorticity and the electrostatics analogy: Ertel-Rossby formulation. *Q. J. R. Meteorol. Soc.*, **121,** 1477-1495

4.5 BAROTROPIC INSTABILITY IN UNIFORM STRAIN

Douglas Parker *

JCMM, University of Reading

1. INTRODUCTION

The role of frontogenetic strain in suppressing the instability of a (potential) vortex strip is an established one. Dritschel *et al.* (1991) (DHJS) showed how a general strain flow will place an upper limit on the growth of linear instabilities to a two dimensional vortex strip. Bishop (1993a,b) and Bishop and Thorpe (1994a,b) confirmed these results for baroclinic basic states representative of atmospheric fronts: although there can be a relatively rapid transient growth of waves, the waves are ultimately suppressed by frontogenetic strain.

Recent objective analyses of UHF (12-36 hour) frontal waves performed by Ayrault *et al.* (1995) (ALJL) using ECMWF data have suggested that there may be two principal classes of frontal wave which affect the UK and Western Europe, denoted 'type 1' and 'type 2'. While type 1 waves may be explained using concepts familiar from the theory of 'primary' baroclinic waves, the type 2 system has more intriguing features, notably a basic state front which lies in markedly *frontolytic* strain. It is the influence of this kind of strain which is considered here, in the case of the two dimensional vortex strip, as a special case of the work of DHJS.

A more detailed study of one of the type 2 cases identified by ALJL, using UKMO Limited Area Model analyses, has shown that the wave develops as it runs along the cold front to meet the triple point of a frontal cyclone. In this configuration, if the warm front is undergoing frontogenetic strain, it is almost inevitable that waves on the cold front experience a frontolytic environment. Thus, the situation of frontolytic strain may, for cold front waves near the triple point, be more generic than might otherwise be surmised, and may even be proposed as a mechanism for triple point development.

* *Corresponding author address*: Dept of Meteorology, University of Reading, Reading RG6 6AU, UK; e-mail <doug@met.reading.ac.uk>.

2. WAVES ON THE FRONTOLYTIC STATE

A primary consideration in this problem is the evolution of the basic state vorticity strip. Any perturbation of the strip orientation from the frontolytic axis will tend to grow with time, and the strip will ultimately approach the frontogenetic axis. This is an objection to the consideration of a frontolytic basic state and it must be shown that frontolysis may persist in the frontal zone for this situation to be of interest. In retrospect it is found that the instability may be rapid compared with the evolution of the basic vortex strip. Here, a negative strain rate is considered, of strength $\gamma < 0$, the front lying along the frontolytic axis for all time.

There are two principal mechanisms for growth in wave-slope of disturbances. The strain field deforms waves kinematically as it thickens the strip and shortens the wavelength, and this implies a kinematic growth rate of -2γ. In addition, there is the familiar barotropic instability mechanism: neutral edge waves on each side of the vortex strip interact to produce a growing mode, provided they are long enough for sufficient interaction to occur. The action of the background strain is to reduce the wavelength progressively, so waves which are initially very long will tend to shorten and increase their possible growth rate (provided they have a suitable structure), but ultimately all waves must pass the short wave cutoff for the system, after which only kinematic growth may occur.

In practice, solving the problem using DHJS's methods, it is found that growth is maximised by transient development at the initial instant (when the structure of the wave, in terms of the phase lag between the edge waves, may be arbitrarily specified). As solutions for different phase lags converge to a single structure, and this structure is in a sense sub-optimal, solutions at later times have a growth rate which is lower than the sum of the kinematic and the maximum barotropic growth rates. However, this growth rate may be considerably larger than the maximum barotropic growth

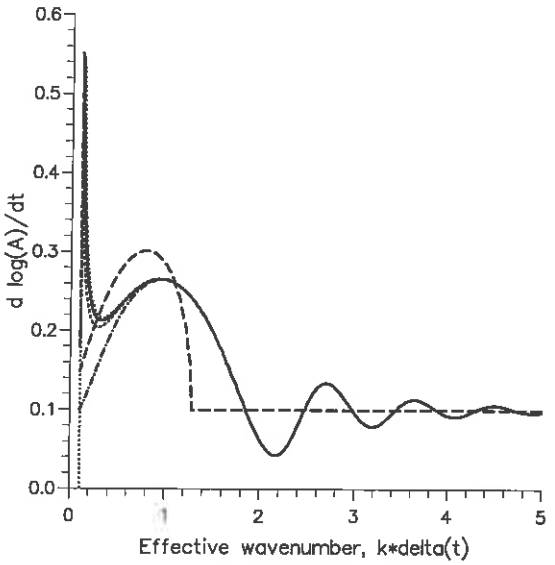

Figure 1: The instantaneous growth rate (scaled with ω) of instabilities on the vortex strip, in a frontolytic flow of strength $\gamma = -0.05\omega$, where ω is the vorticity of the strip. The effective wavenumber increases exponentially as $k\Delta = \exp(-2\gamma t)$. Curves are for different initial phase lags; the solid curve gives the maximum possible growth at a given time while the dashed curve is an instantaneous estimate found as the sum of the kinematic growth rate and the normal mode growth rate at given wavenumber.

rate in the absence of a background strain flow (figure 1).

Growth is maximised at the initial time because the structure of the wave may be specified freely at this point. This suggests that the greatest growth rate may only be attained for a limited time.

3. CONSEQUENCES

Typical atmospheric values of the strain parameter may be greater than $10^{-4}s^{-1}$, implying a kinematic growth rate of disturbances of twice this value, roughly 20 day^{-1}, for waves on a suitably-oriented front. This is a large growth rate for frontal waves, and as it has been seen that the transient barotropic growth may further increase the growth rate of disturbances with suitable structure, the presence of negative strain at a front may be important for explosive development. However, the barotropic vortex strip is only the simplest analogue for an atmospheric front and further investigation of baroclinic systems needs to be done. In particular, it is arguable whether the measure of growth of waves used in this study, that of wave slope, is the most useful for assessing the growth of frontal waves. Several other parameters may be of more importance in the atmospheric context; vorticity amplitude (for baroclinic instabilities), maximum vertical velocity or maximum surface wind speed are other contenders.

Acknowledgement

This work has been supported by NERC grant GR3/9036.

REFERENCES

Ayrault, F., Lalaurette, F., Joly, A. and Loo, C., 1995, 'North Atlantic ultra high frequency variability. An introductory survey', *Tellus*, **47A**, 671-696.

Bishop, C.H., 1993a, 'On the behaviour of baroclinic waves undergoing horizontal deformation. Part I:The "RT" phase diagram', *Q. J. R. Meteorol. Soc.*, **119**, 221-240.

Bishop, C.H., 1993b, 'On the behaviour of baroclinic waves undergoing horizontal deformation. Part II: Error bound amplification and Rossby wave diagnostics', *Q. J. R. Meteorol. Soc.*, **119**, 241-269.

Bishop, C.H. and Thorpe, A.J., 1994, 'Frontal wave stability during moist deformation frontogenesis. Part I: Linear wave dynamics', *J. Atmos. Sci.*, **51**, 852-873.

Bishop, C.H. and Thorpe, A.J., 1994, 'Frontal wave stability during moist deformation frontogenesis. Part II: The suppression of non-linear wave development' *J. Atmos. Sci.*, **51**, 874-888.

Dritschel, D.G., Haynes, P.H., Juckes, M.N. and Shepherd, T.G., 1991, 'The stability of a two-dimensional vorticity filament under uniform strain', *J. Fluid Mech.*, **230**, 647-665.

MESOSCALE STRUCTURES IN BAROCLINIC LIFE CYCLES

J Methven* and B J Hoskins

Dept of Meteorology, University of Reading, U.K.

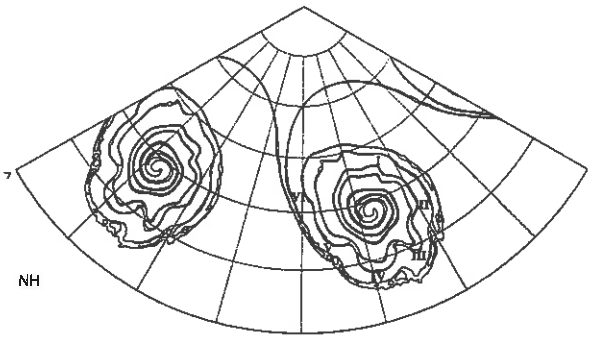

Figure 1: Diagnosed PV on the 300K surface at day 9 of the T341 simulation of the LC2 experiment. Only the $1.5\,PVU$ and $2.0\,PVU$ contours are shown. The Roman numerals label the disturbances in age order.

1. INTRODUCTION

The instability and subsequent roll-up of PV filaments is a commonplace occurrence in the mid-latitudes. At upper levels such PV anomalies are associated with tropopause troughs. The trough shape has an impact on the dynamics of the filament. For instance, troughs which have a deep aspect ratio ($\frac{H}{L} \gg \frac{f}{N}$) are expected to behave quasi-barotropically. Such instabilities can be suppressed by background adverse shear and strain.

Here the baroclinic wave life cycle experiments of Thorncroft *et al.* (1993) are revisited at much higher resolution (T341, L30). Many of the narrow filaments were observed to be unstable but in this abstract the focus will be on the spiral in PV which occurs in the LC2 experiment (Figure 1).

2. INSTABILITY OF A SPIRAL IN PV

The signature of the instability is revealed by the undulations of PV on the 300K isentropic surface. The angular velocity of the disturbances ($\approx$) $\pi\,rad\,day^{-1}$, making them approximately stationary with respect to the background flow. The instability has a well defined wavelength ($\approx 600\,km$) which hardly changes with time, whilst the undulation amplitude was found to increase exponentially from day 8 to day 9 with a growth rate of $2.2\,day^{-1} \pm 0.2\,day^{-1}$. After this time the disturbance saturated nonlinearly and the rate of amplitude increase slowed.

Disturbances which bear a strong resemblance to these filamentary instabilities have been observed in the atmosphere. For example, Ralph (1995) observed, using satellite imagery, a set of five $750\,km$ wavelength cyclonic disturbances wrapped around a synoptic scale cyclone.

The background state upon which the filamentary instability grows is, to a good approximation, given by the T85 life cycle, for which the instability is absent. At T85 resolution, the LC2 vortex appears as a nearly homogeneous PV blob. The associated winds are, however, capable of accurately reproducing the structure of the high resolution spiral in PV, before the growth of filamentary instability, using the contour advection technique (Methven, 1996) . In addition, the evolution of globally averaged eddy kinetic energy is virtually unchanged by increased resolution (the difference between the life cycles at T341 and T85 resolution is, at most, 2%). This wind field is almost axisymmetric and the radial shear in angular velocity is given by $S = r\frac{d\omega}{dr}$. The wind shear is described as "adverse" if it opposes the shear in angular velocity induced by the vorticity strip itself ($S < 0$). The strain experienced by a fluid element during the growth of instability is given by the finite time Lyapunov exponent. Values for strain experienced by the high PV filament were calculated using domain filling trajectories and were found to be less than $1.2\,day^{-1}$ except for the outermost turn of the spiral; this turn experienced the strain due to the vortices upstream and downstream.

The observed growth rate and wavelength of the disturbance were compared with the predictions of a linear stability analysis for a straight, uniform, isolated strip of vorticity in a barotropic flow, using the observed magnitude and width of the PV anomaly. Table 1 shows the results for three cases: instability in the absence of shear or strain, instability in the greatest adverse shear experienced by the filament (Dritschel, 1989) , and instability in the maximum effective strain (Dritschel

*Corresponding author: Dept of Meteorology, University of Reading, 2 Earley Gate, Whiteknights, Reading, RG6 2AU, U.K.

et al., 1991).

In the LC2 vortex the nature of the inversion operator, the cross-strip vorticity distribution and interactions with neighbouring coils of the spiral all act to reduce growth rates (Dritschel (1989), Waugh and Dritschel (1991)). However their combined effect reduces the predicted growth rate by less than 15%. In addition, the curvature of the LC2 filaments is expected to make them more unstable than predicted for straight filaments thus partly counteracting the reduction in growth rate due to the other factors.

Whilst the PV anomalies are deep, they do not extend to the ground or very far into the stratosphere (Figure 2). Juckes (1995) considered the instability of shear lines associated with upper-tropospheric PV anomalies in the opposite extreme where the undulations of the tropopause are shallow. The dynamics of such a shear line can be described by quasi-geostrophic tropopause dynamics (Juckes, 1994) ; the range of interaction between anomalies is shorter than for barotropic dynamics so that although the instability growth may be slower the likelihood of suppression of instability by nearby large scale vortices is also smaller. Table 1 shows that the growth rates are almost three times lower than the observed growth rate of the instability. Also the wavelengths of these instabilities are over twice as long as observed.

		σ_{eq} (day^{-1})	Wavelength (km)
Observed		2.2	600
Barotropic dynamics	$V_b = 0$	4.2	790
	max shear	2.2	570
	max strain	1.9	420
QG tpp	$V_b = 0$	0.8	1200

Table 1: The growth rate and wavelength of the most unstable normal modes for different flows. V_b refers to the background velocity. For the maximum strain case σ_{eq} is the equivalent growth rate for the mode which amplifies most in a finite time (here 1.0 *day*).

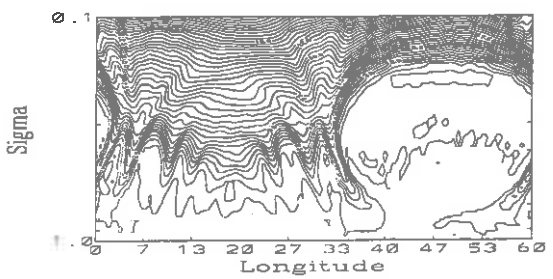

Figure 2: Section through the spiral centre (49N) at day 9 showing PV-like tracer with log-pressure as the vertical coordinate; the axes are scaled so that anomalies with a horizontal to "vertical" aspect ratio of N/f would appear to have an aspect ratio of 1 on the plot. Note that the PV-like tracer was initialised as PV at day 0 and the contour interval is 0.5 PVU.

3. CONCLUSIONS

The predictions of barotropic instability theory were demonstrated to be more applicable to the LC2 case than quasi-geostrophic tropopause dynamics, provided that suppression of growth rates by adverse shear and strain were accounted for. This was expected because the unstable PV anomalies were extremely deep ($\frac{NH}{fL} \sim 4$) and had little tilt. The outermost turn of the PV spiral was baroclinic in nature (associated with a tilted fold and steep isentropic surfaces) but the instability was suppressed by the strain of neighbouring vortices.

References

Dritschel, D. (1989). On the stabilization of a 2-D vortex strip by adverse shear. *J.Fluid Mech.*, **206**, 193–221.

Dritschel, D., Haynes, P., Juckes, M., and Shepherd, T. (1991). The stability of a 2-D vorticity filament under uniform strain. *J.Fluid Mech.*, **230**, 647–665.

Juckes, M. (1994). Quasigeostrophic dynamics of the tropopause. *J.Atmos.Sci.*, **51**, 2756–2768.

Juckes, M. (1995). Instability of surface and upper-tropospheric shear lines. *J.Atmos.Sci.*, **52**, 3247–3262.

Methven, J. (1996). *Tracer behaviour in baroclinic waves.* Ph.D. thesis, Reading University.

Ralph, F. (1995). Observations of 250 *km* wavelength clear-air eddies and 750 *km* wavelength mesocyclones associated with a synoptic-scale mid-latitude cyclone. *Mon.Wea.Rev.*, **accepted.**

Thorncroft, C., Hoskins, B., and McIntyre, M. (1993). Two paradigms of baroclinic-wave life-cycle behaviour. *Quart.J.Roy.Met.Soc.*, **119**, 17–55.

Waugh, D. and Dritschel, D. (1991). The stability of filamentary vorticity in 2-D geophysical vortex dynamics models. *J.Fluid Mech.*, **231**, 575–598.

5.18 VARIATION OF FRONTAL AND PRECIPITATION STRUCTURE ALONG A COLD FRONT

Keith A. Browning and Nigel M. Roberts *

Joint Centre for Mesoscale Meteorology
University of Reading, UK

1. INTRODUCTION

A diagnostic study is presented to illustrate the sequence of events in which a warm-conveyor-belt flow (WCB) is drawn into the circulation of a developing extratropical cyclone and interacts with dry air aloft to produce distinctive precipitation structures. The poleward boundary of the upstream end of the WCB was associated with a classical (ana-) cold frontal structure. The other end of the WCB flow, closer to the cyclone centre, was overrun by a 'dry intrusion' of low-θ_w air to give a split (kata-) cold front. The orientation of the surface cold front (ie the WCB boundary) changed significantly between these two parts. The surface cold front was characterised in most places by a narrow cold frontal rainband composed of shallow line convection elements (James and Browning 1979) or precipitation cores (Hobbs and Biswas 1979) aligned nearly parallel to the

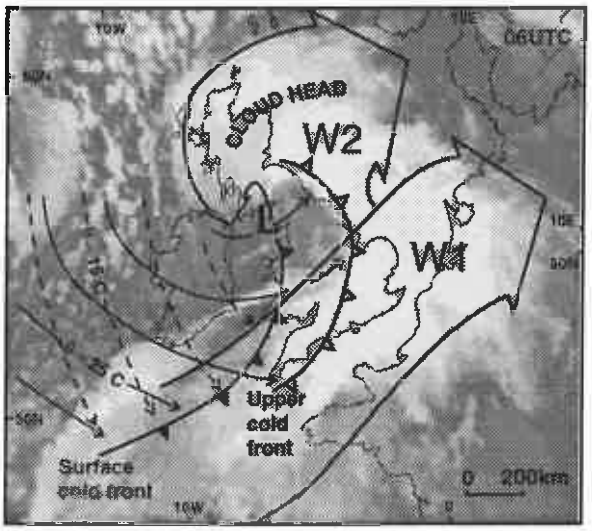

Figure 1. Meteosat infrared image for 06 UTC, 8 Dec 1994. Grey shades denote brightness temperatures as follows: lightest grey < -44°C, grey shade interval 6°C, darkest grey > 4°C. Superimposed is the system-relative flow on the θ = 25°C (thin solid lines) and θ = 15°C (thin dashed lines) isentropic surfaces, associated with the dry intrusion. The warm coveyor belts (high-θ_w air) are shown as flows W1 and W2. The low centre is marked with an L.

* *Corresponding author address:* Nigel M. Roberts, Joint Centre for Mesoscale Meteorology, Harry Pitt Building, University of Reading, PO Box 240, Reading, England, RG6 2FN; e-mail <nmroberts@meto.govt.uk>

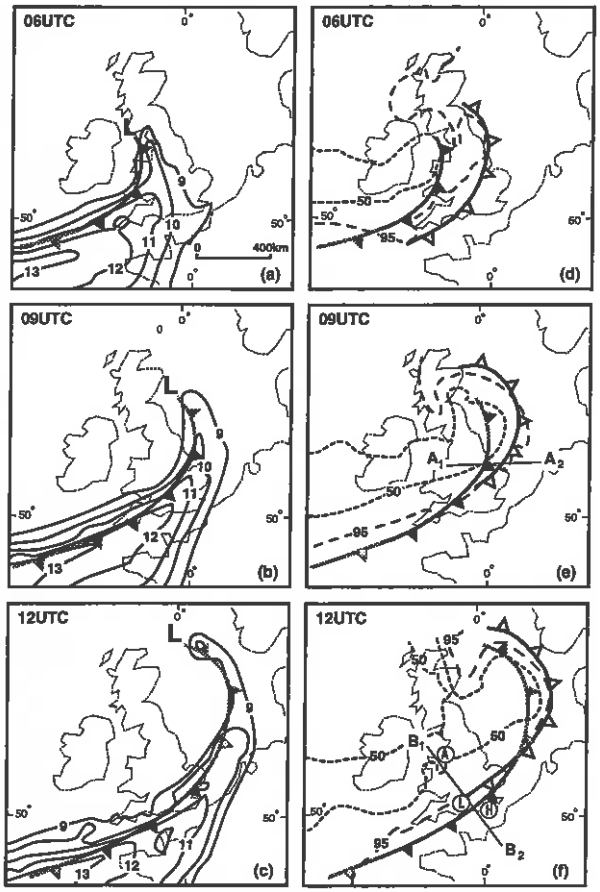

Figure 2. Left hand panels show θ_w at 950 mb for (a) 06, (b) 09 and (c) 12 UTC, 8 December 1994, derived from the 06 UTC run of the UK Met Office operational mesoscale model. Isopleths are at 1°C intervals above 9°C. The low centre is marked L. The surface front is drawn black when based on detailed radar and surface observations; elsewhere it is drawn grey. Right hand pannels (d), (e) and (f) show the dry intrusion at 600 mb from the same model run. Isopleths are shown for 95 and 50% relative humidity. The upper humidity front is depicted with open symbols. Also shown in (e) is the location A_1 A_2 of the section in figure 3 and in (f) the location B_1 B_2 of the section in figure 4. Radiosondes used in section B_1 B_2 are marked Ⓐ, Ⓛ and Ⓗ.

surface geostrophic flow in the WCB. It is shown that the changing relationship between the frontal orientation and the direction of the surface flow accounts for the fact that the line convection elements occurred end-to-end to give almost 2-d line convection along the classical ana part of the cold front, but were non-aligned and widely spaced along the split cold front part.

2. THE OVERALL STRUCTURE

Figure 1 shows the frontal analysis and the airflow relative to the movement of the low centre, in relation to the cloud pattern associated with the developing cyclone. The overall configuration was established by the interaction of a low-level baroclinic zone with an upper-level potential-vorticity maximum and tropopause fold. The latter was accompanied by a 'dry-intrusion' of low-θ_w air advancing from the west (see figures 2(d), (e) and (f)). In the northern part of the system, within several hundred kilometres of the cyclone centre, the dry intrusion overrode a narrowing tongue of relatively high-θ_w air (see figures 2(a), (b) and (c)) and advanced ahead of the surface cold front to give a structure consistent with the split-cold-front model of a kata-cold front (see figure 3). Farther south, in the trailing part of the cold front, the dry low-θ_w air undercut rearward-ascending high-θ_w air to give a classical ana-cold front (see figure 4).

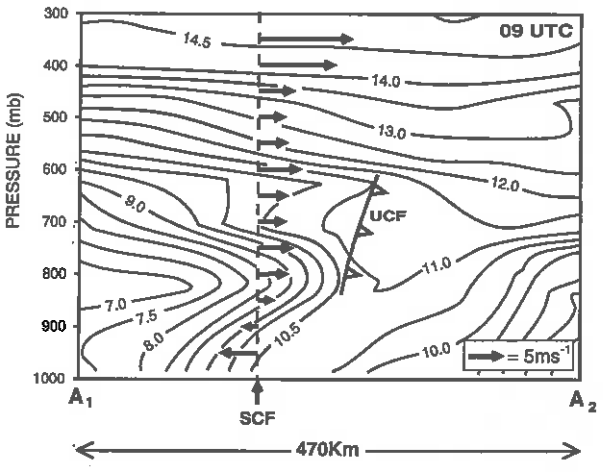

Figure 3: Cross section along $A_1 A_2$ in figure 2(e) for 09 UTC, 8 December 1994, derived from the 06 UTC forecast run of the UK Met Office operational mesoscale model. Contours are of wet-bulb potential temperature at 0.5°C intervals. Wind arrows above the surface cold front (SCF) show model-derived relative wind components normal to the SCF. The upper cold front (UCF) is depicted as a line with open symbols.

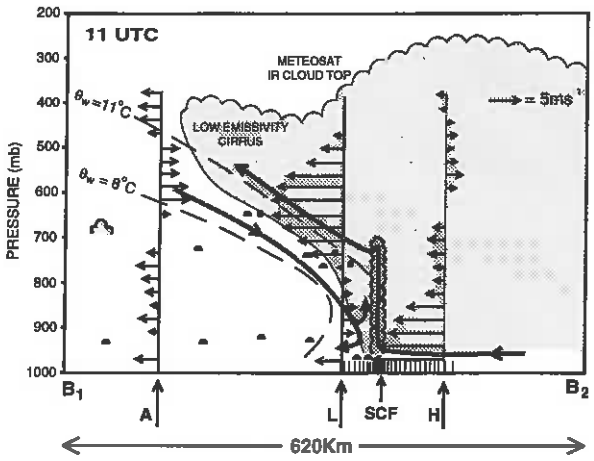

Figure 4. Cross section, along $B_1 B_2$ in figure 2(f) for 11 UTC, 8 December 1994, derived from observations alone. Dashed contours show $\theta_w = 8°C$ and 11°C derived from radiosondes at A, L and H (figure 2(f)); horizontal arrows show front-normal wind components relative to the front derived from the same radiosondes; vertical hatching denotes surface rainfall with spacing proportional to rainfall intensity; columnar feature above the heaviest rain is line convection as observed by radar; shaded region represents cloud as inferred from infrared imagery and surface observations; circles and semicircles show individual observations of total and partial cloud cover, respectively; bold arrows show schematic ana-cold front circulation.

3. THE NARROW COLD FRONTAL RAINBAND

The transition between the split-front and classical-front parts of the cold front was marked by a change in the structure of the narrow cold frontal rainband that occurred along the surface front. Everywhere the narrow cold frontal rainband was due to a very narrow band of strong updraught, less than 3 km deep, ie line convection. However, there was a transition from almost continuous 2-dimensional line convection in the region of the classical cold front to distinctly broken line convection elements, oriented at 30 deg to the mean direction of the surface cold front, in the region of the split-cold front (fig 5). Individual line elements broke away from the northern end of the continuous line convection within the classical part of the front and advanced into the split-cold front part where they could be tracked as broken line elements for over 4 hours. This transition to broken line elements was associated with a change in the orientation of the surface cold front with respect to the preferred orientation of the convective line elements (fig 5): it was not due to the change in the orientation of the line elements themselves, because this was small by comparison. Thus the observed behaviour in this case is inconsistent with a

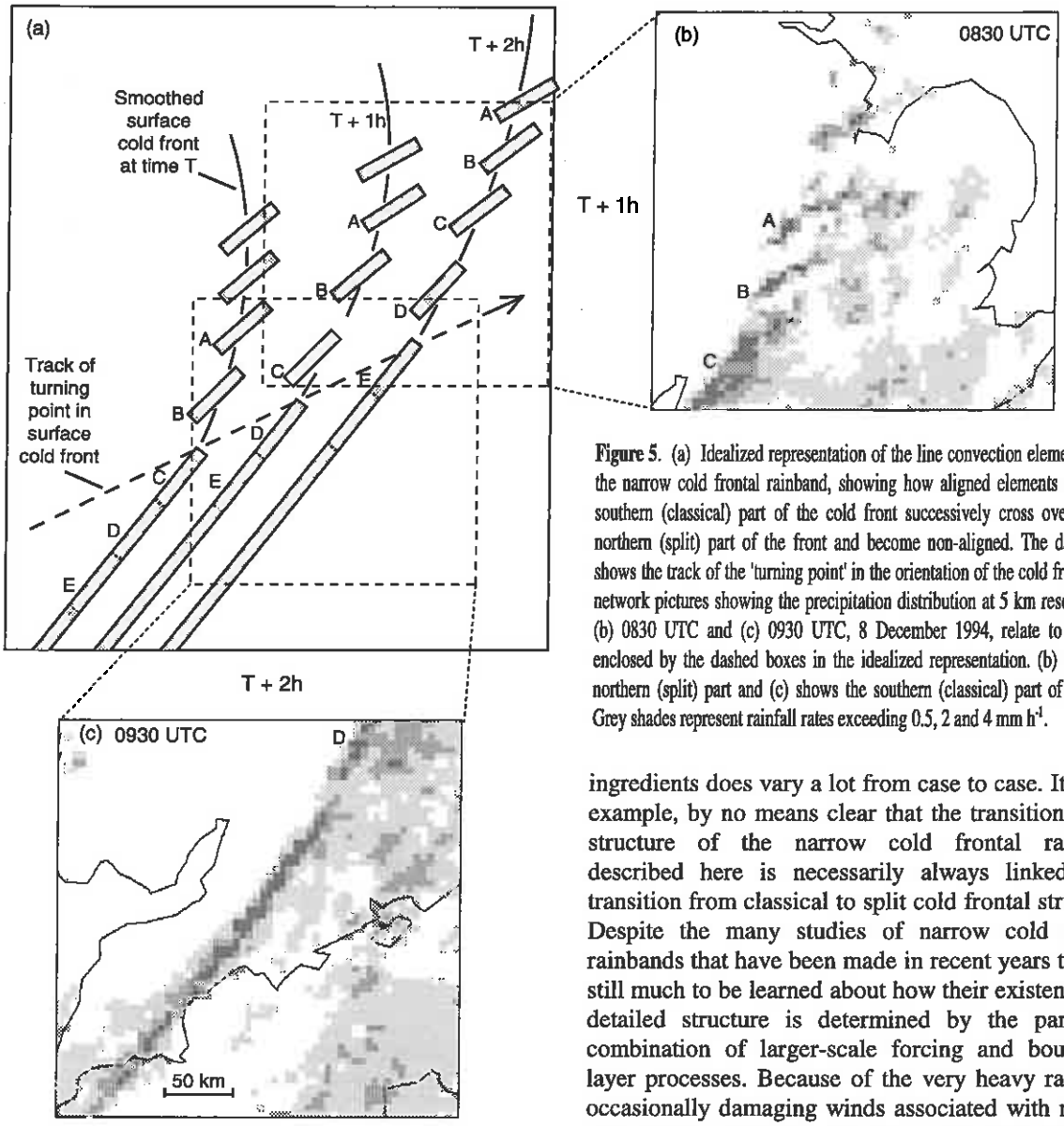

Figure 5. (a) Idealized representation of the line convection elements within the narrow cold frontal rainband, showing how aligned elements within the southern (classical) part of the cold front successively cross over into the northern (split) part of the front and become non-aligned. The dashed line shows the track of the 'turning point' in the orientation of the cold front. Radar network pictures showing the precipitation distribution at 5 km resolution for (b) 0830 UTC and (c) 0930 UTC, 8 December 1994, relate to the areas enclosed by the dashed boxes in the idealized representation. (b) shows the northern (split) part and (c) shows the southern (classical) part of the front. Grey shades represent rainfall rates exceeding 0.5, 2 and 4 mm h^{-1}.

mechanism in which shearing instabilities lead to the creation of strongly segmented elements of line convection solely by the reorientation of sections of an initially 2-dimensional strip of line convection (Matejka 1980).

4. CONCLUDING REMARKS

The structure of an individual cold front can vary significantly in both space and time and the 2-dimensional approach used in many theoretical studies of frontogenesis might not always be an appropriate idealisation. Although the particular frontal configuration described is thought to be fairly common at least in the UK, the detailed mix of ingredients does vary a lot from case to case. It is, for example, by no means clear that the transition in the structure of the narrow cold frontal rainband described here is necessarily always linked to a transition from classical to split cold frontal structure. Despite the many studies of narrow cold frontal rainbands that have been made in recent years there is still much to be learned about how their existence and detailed structure is determined by the particular combination of larger-scale forcing and boundary-layer processes. Because of the very heavy rain and occasionally damaging winds associated with narrow cold frontal rainbands, this is an important practical problem as well as an intriguing research topic requiring further attention.

References

Hobbs, P. V. and K. R. Biswas, 1979: The cellular structure of narrow cold frontal rainbands. *Quart. J. Roy. Meteor. Soc.*, **105,** 723-727.

James, P. K. and K. A. Browning, 1979: Mesoscale structure of line convection at surface cold fronts. *Quart. J. Roy. Meteor. Soc.*, **105,** 371-382.

Matejka, T. J., 1980: Mesoscale organisation of cloud processes in extratropical cyclones. PhD thesis, University of Washington, 361pp.

P5.27 FRONTS 92 IOP 1 - MESOSCALE STRUCTURES ASSOCIATED WITH SNOW SUBLIMATION

S A Clough[1]*
Joint Centre for Mesoscale Meteorology,
*UK Meteorological Office / University of Reading, UK.

1. INTRODUCTION

Mesoscale observational studies of frontal weather systems tend to concentrate upon low pressure centres and cold fronts, where largest gradients occur in association with intense features such as mesoscale vortices. However, from a cloud physical point of view the warm sector and warm frontal regions hold considerable interest. They are more usually associated with deep cloudy layers where the influence of phase changes may be expected to be large. From the point of view of observation the upper regions hold the practical advantage that they are well separated from the earth's surface. Thus they are less prone to the distortion that leads to small-scale 3-dimensional structures. as at cold fronts. It thus seems likely that mesoscale structure in these regions may be more precisely understood in terms of elementary physical processes. Since these processes are increasingly the focus of forecast and climate model parametrizations, such studies are likely to have practical utility also.

The primary microphysical processes operating within and around such deep frontal clouds are deposition and riming growth, aggregation, sublimation and melting. A number of studies of the microphysics of such frontal clouds have emphasised the possibility that mesoscale structure might be associated with an interplay of heating and cooling associated with these processes. In the regime above the melting level, which is the primary topic of this work, sublimation is the only microphysical process likely to lead to substantial cooling of the atmosphere within and below cloud.

There appear to be two paradigms in the literature for the operation of sublimation to cause mesoscale structure such as precipitation bands. Clough and Franks (1991) demonstrated that the mesoscale dynamical effects of snow sublimation are usually more important than those of rain evaporation in mid-latitude frontal systems because of the low bulk density and terminal velocity of large ice crystals. Using a simple 1-dimensional model they showed that sublimation could maintain near-saturation in frontal clouds subject to imposed descent at up to 30 cms^{-1}. Thus they suggested a steady state paradigm, in which mesoscale circulations might be more readily supported above or within the melting layer. This led them to suggest that sublimation was sufficiently rapid to offset subsidence warming in CSI or similar mechanisms leading to mesoscale circulations, a conclusion which has been supported by subsequent observational studies (eg. Barth and Parsons (1995), Marecal and Lemaitre (1995)).

However, an earlier paradigm exists for the dynamical effects of sublimation. Using radar observations and 1-dimensional microphysical model calculations, Harris (1977) demonstrated that sublimation of ice crystals falling from cirrus, ie. virga, was so rapid that it was capable of causing static instability and turbulent downdraughts in dry air beneath the cloud deck. Thus the microphysical heat conversion through precipitation and sublimation is not just keeping pace with the dynamics, but is way ahead, driving the thermodynamic structure locally. While this virga paradigm was not emphasised by Clough and Franks, it is fully consistent with the shallow sublimation depth scales given by their calculations.

The FRONTS 92 experiment (Hewson,1993) was devoted to the study of developing frontal waves using the UKMO C130 aircraft and dropsondes. The observations made in IOP 1 of the experiment were made in a region encompassing such a deep upper cloud layer and its' interface with drier air in the descending outflow from a ridge. These conditions provide an ideal opportunity see mesoscale evidence of virga sublimation in practice.

2. OBSERVATIONS

2.1 *Synoptic environment.*

IOP 1 of FRONTS 92 was carried out on 17th March 1992, to study a wave to the west of the UK. (Figs. 1 and 2) The progression of the wave was impeded by the development of the weak low centre at 48° 35°W, and dropsonde runs shown in Fig. 2 did not reach the surface cold front, but were placed in a complex, cloudy region of the system evident from the surface analysis and satellite image. Three runs were made in a zig-zag pattern over a 4 hour period; the run numbering is indicated in Fig. 2. Fig. 3 shows the pattern of individual soundings, in an area where the cloud tops range from -50C to about 5C, marking the transition from

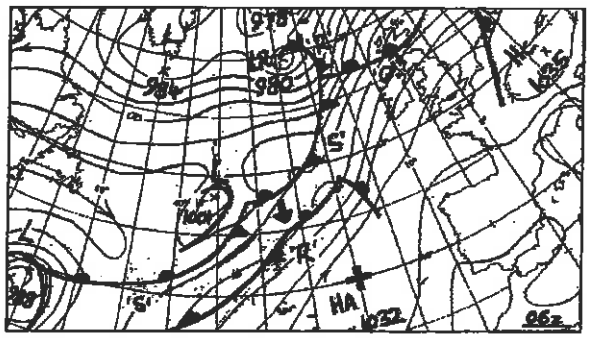

Figure 2 Surface analysis for 06UT 17 March 1992 from UKMO Central Forecast Office.

[1] Joint Centre for Mesoscale Meteorology, Harry Pitt Building, University of Reading, Whiteknights Road, PO Box 240, Reading, RG6 2FN, UK. (The Joint Centre for Mesoscale Meteorology is supported by the Meteorological Office and the Department of Meteorology, University of Reading.)

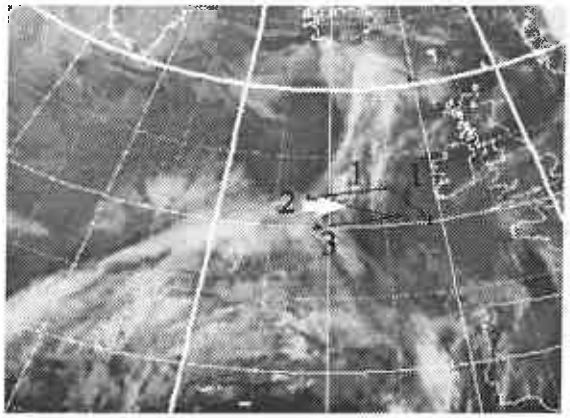

Figure 2 Meteosat infrared image for 06UT on 17th March 1992 with the track of the C130 aircraft dropsonde runs indicated.

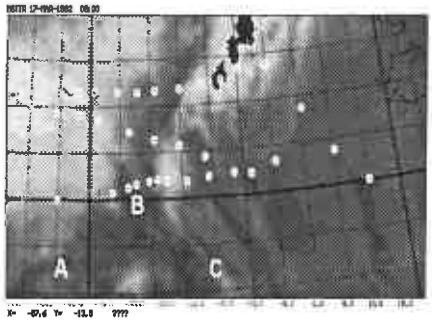

Figure 3 Meteosat infrared image for 09UT on 17th March 1992. Dropsonde positions are indicated with circles.

the deep ascending moist warm conveyor belt flow into cooler drier air descending downstream of the ridge. This transition is marked in the relative humidity pattern of all three runs by a forward-sloping moist overhang in mid-troposphere, as shown in Fig. 5 below.

The runs penetrate a region where the soundings show a warm frontal zone north of that indicated on the analysed chart (Fig. 1). The arc ABC in Fig. 3 coincides with an area of dissipation in the cloud where animations of satellite imagery indicate anticyclonically curving descent behind the warm front.

Fig. 4 shows a tephigram of the final sounding of run 3, placed in some of the deepest cloud encountered. The stable/unstable temperature pattern beneath the upper cloud deck is typical of the structures anticipated from the model of Harris (1977), which predicted destabilisation proportional to precipitation rate. (In ice cloud precipitation rate may be qualitatively expected to increase with cloud depth.) A similar structure is also evident in the westernmost sounding of run 1 (not shown), whereas the remaining soundings show very weak stability in the layer immediately beneath cloud.

2.2 *Cross-section structure*

Cross-sections were produced from each run in turn, and are shown in a plane perpendicular to the thermal wind (20°E of N); vector quantities were evaluated with y axis along the thermal wind and a two-dimensional assumption. Although it is clear from the imagery that there is substantial three dimensionality in the system on the large scale, the mesoscale structures discussed here are found to be common to 2 or 3 runs, and patterns qualitatively insensitive to rotation of this axis by 20° in either direction.

Fig. 5 shows the static stability and relative humidity pattern from run 3. Around 4 to 5 km the interface between the moist overhang and drier air is marked by a pronounced transition from high static stability (>7 K/km) at cloud base to a layer of low values(<2 K/km) within a few hundred metres. The lower region is also marked by rather small windshear, which is consistent with increased mixing due to turbulence in the sub-cloud layer, as indicated in Harris's doppler radar observations. The sloping layers maintain this intensity over about 150 km of the cross-section, though the broader stable/unstable band extends over most of the section, and is present in all 3 runs.

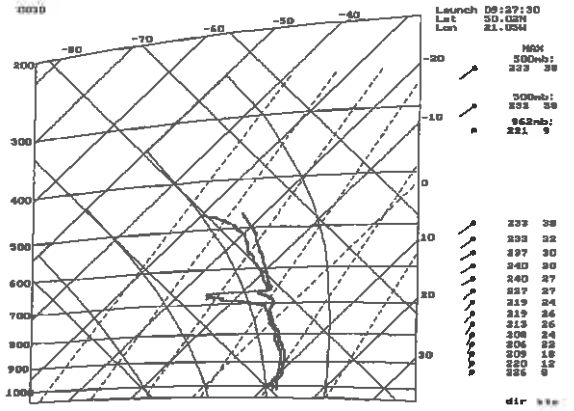

Figure 4 Tephigram showing the westernmost sounding of run 3.

The thermodynamic signatures are accompanied by consistently defined characteristics in other properties of the independently measured velocity fields. For example, the sloping transition from moist to dry air is also marked by a transition from higher horizontal shear vorticity within the upper cloud edge to lower values in the drier air below (not shown).

Fig. 6 shows the associated potential vorticity cross-section (evaluated with a 2-dimensional approximation). The vorticity transition and the static stability change correspond to a high PV value in the lower part of the cloud overlying a rather low minimum

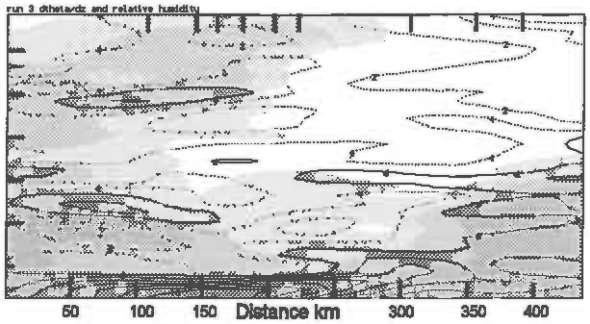

Figure 6 Static stability dθ/dz from run 3 (contoured at intervals of 2°C km^{-1}, solid for 6°C km^{-1} and above, dashed below) overlaid upon relative humidity (shaded with thresholds at 30%,60%,90%). Left had tick marks are at 1 km intervals, while upper ones denote sounding locations.

value in the dry air.

This signature is particularly interesting in that the simplest conceptual model of warm sector cloud, andalso typical forecast model diagnostics in our experience, tend to imply low potential vorticity values within upper cloud because the maximum latent heating occurs at lower levels where most of the latent heat release occurs. While such a pattern may reasonably expected in the synoptic scale mean value, however, these observations suggest that the mesoscale potential vorticity field is rather more complex and also is sensitive to microphysical processes. It may thus provide a useful diagnostic for comparison with the bulk effects of ice precipitation predicted from model parametrization schemes.

Two cautions must be added, however. Firstly this evidence is circumstantial, since no direct precipitation observations were possible in this case (though both the meteorological situation and the evolution seen in the satellite imagery are consistent with the given interpretation). Other information such as radar reflectivities and/or in situ particle data are essential to provide sufficient constraints to validate model parametrizations. The second caution concerns the limited accuracy possible in the evaluation of both mesoscale vertical velocity and potential vorticity from soundings, though GPS wind-finding and/or suitable doppler radar observations may improve on current performance.

3. DISCUSSION

The case discussed above appears to verify the important role for sublimation suggested by the microphysical calculations of Harris (1977) and Clough and Franks (1991). Precipitation data are not available, but the observations from FRONTS 92 IOP 1 suggest that sublimation of snow can produce extensive layers of high and low static stability similar to those discussed by Harris. The situation considered here compares more closely with the virga paradigm of Harris than the steady state case considered by Clough and Franks. The thermodynamic signatures are reflected also in a near-vertical dipolar potential vorticity pattern, with high values in the overlying moist air.

Since sublimation occurs most strongly in the descending outflow downstream of the ridge of a weather system the resulting mesoscale potential vorticity pattern must remain in the airmass while it remains under adiabatic clear air conditions. However, if such an airmass were later subjected to ascent in a developing weather system it is quite possible that the patterns observed at the later stage will show the mesoscale potential vorticity structure which has been etched into them during descent (though clearly distorted by any deformation they may suffer during development).

This possibility raises an interesting difficulty for the study of mesoscale structures such as rainbands or cloud bands, which tend to be interpreted in terms of hypothesised processes such as CSI occurring in the developing system rather than the unobserved previous history.

At this point, however, the results above are in a degree speculative in lack of validating microphysical or radar observations. The combination of dropsonde observations with in situ and radar observations envisaged in experiments such as FASTEX offer promising opportunities to provide more precise validation.

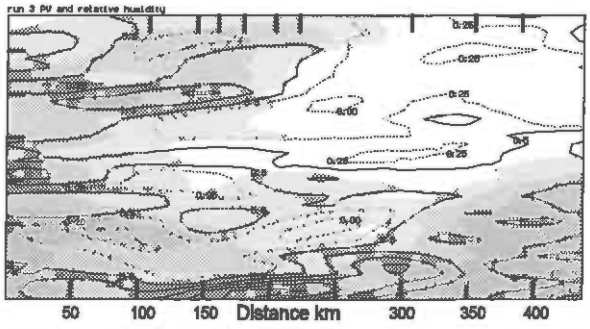

Figure 6 PV in a 2-d approximation (units of 10^{-6} m^2 s^{-1} K kg^{-1}) for run 3, overlaid on relative humidity. Other aspects as Fig. 5.

REFERENCES

Barth, M. C. and D. B. Parsons, 1995: Microphysical processes associated with intense frontal rainbands and the effect of evaporation and melting on frontal dynamics. submitted to *J. Atm. Sci.*

Clough, S. A. and R. A. A. Franks, 1991:The evaporation of frontal and other stratiform precipitation. *Quart. J. R. Meteor. Soc.*, 117, 1057-1080.

Harris, F. I., 1977: The effects of evaporation at the base of ice precipitation layers: theory and radar observations. *J. Atm. Sci.*, **34**, 651-672.

Hewson, T. D., 1993: The Fronts 92 Experiment: a Quicklook Atlas. JCMM Internal Report No. 15, 176pp.

Marecal, V. and Y. Lemaitre, 1995: Importance of microphysical processes in the dynamics of a CSI mesoscale frontal rainband. *Quart. J. R. Meteor. Soc.*, 121, 301-318.

P6A.1

3D RADIATIVE-CONVECTIVE EQUILIBRIUM IN THE TROPICAL ATMOSPHERE

A. M. Tompkins* and G. C. Craig

Joint Centre for Mesoscale Meteorology, University of Reading,

1. INTRODUCTION

A knowledge of radiative-convective interactions is key to an understanding of the tropical climate. Convection heavily influences the water vapour profile in the clear-air environment. Water vapour, the most important greenhouse gas, affects the infra-red radiative cooling of the clear-air environment, which in turn determines the clear-air subsidence mass-flux. The convective mass-flux is constrained to balance this clear-air subsidence (with large-scale convergence/divergence taken into account) and so it is obvious that the possibility for significant radiative-convective feedback exists.

If these interactions are to be closely examined using models, these model need to include a best possible representation of all the relevant physics that could be involved. Therefore it can be argued that General Circulation Models (GCMs), containing parameterizations for convection and cloud amounts are not entirely suitable for this purpose. Instead cloud resolving models, with better representations of cloud microphysics, can be used to study convection in statistical equilibrium with its environment, given set boundary conditions.

Held et al. (1993) (referred to in future as H93) and Lau et al. (1993) (referred to as L93) have previously studied radiative-convective equilibrium states, with two-dimensional (2D) cloud resolving models, and the sensitivity of this state to an increase in the fixed imposed underlying surface temperature. Both reported little change in lower tropospheric relative humidity (RH) in response to a surface warming. In the upper troposhere, H93 found a decrease in RH in response to a surface warming, in contrast to L93 who reported an increase.

Modelling in two dimensions places a constraint on the dynamics of convection and so a three dimensional model is required. Robe and Emanual (1995) and Islam et al. (1993) have both operated 3D cloud models to an equilibrium state, but in both cases a fixed radiative cooling was imposed and simple microphysics used.

A three-dimensional cloud ensemble model, with a fully interactive radiation scheme, and three phase microphysics, has now been run to a radiative-convective statistical equilibrium state. This paper aims to briefly outline the setup used for this initial experiment, and report a few characteristics of this equilibrium state.

* *Corresponding author address*: Adrian Tompkins, Department of Meteorology, University of Reading, 2 Earley Gate, Whiteknights, Reading, Berkshire, United Kingdom, RG6 2AU; e-mail A.M.Tompkins@rdg.ac.uk

2. MODEL

The basic cloud model used in this experiment is based on an anelastic equation set, and is detailed in Shutts and Gray (1994). The model includes a three phase microphysical scheme with prognostic equations for rain, snow, cloud water, cloud ice and graupel (Swann, 1993), and an advanced total variation diminishing scheme for advection of all prognostic quantities. The radiation scheme that has been added to the model calculates heating rates for both the shortwave and infrared spectrums dividing the former into nine bands and the latter into six. It is based on the two-stream approximation and outlined in Edwards and Slingo (1996). The scheme takes the mixing ratios of the microphysical quantities into account when calculating heating rates. The mixing ratios also alter the effective radius used following Petch (1995). The radiation scheme is called every 120 timesteps; equivalent to an average of every 18 minutes. This is shorter than the cumulus timescale in an attempt to eliminate 'ghost clouds' in the forcing. The solar zenith angle used is 51.7° to ensure a realistic path-length, with an appropriate 'length of day' factor added to make the solar constant 685 W m^{-2}. The surface fluxes of water vapour (q_v) and heat are calculated using a formulation based on Monin-Obukhov theory. No minimum surface wind speed is imposed.

The domain size used for the experiment is 100km by 100km in the horizontal and 20km in the vertical. This domain size is large enough to continuously include at least one deep convective event throughout the integration, although in reality there are usually several deep-convective events of varying stages of maturity occurring at any particular time (Figure 1). The horizontal resolution is chosen to

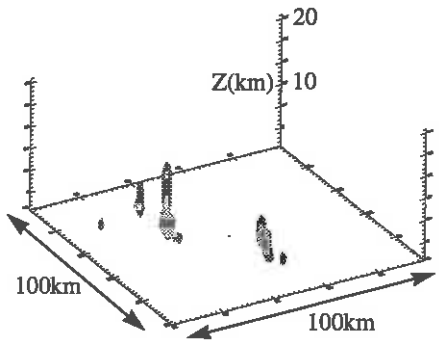

Figure 1. Snapshot of regions within the domain with vertical velocity exceeding + 1ms^{-1} at day 50 of the integration. Note the existence of several convectively active regions within the domain. This snapshot is representative of the entire integration.

marginally resolve convection at 2km, and the vertical grid consists of 30 levels, with Δz ranging from 183m at the surface to approximately 1.5km at the top of the domain. The first model half-level is set at 40m above the surface. The vertical velocity is set to zero at the bottom and top of the domain, and the lateral boundary conditions imposed are cyclic. A Newtonian damping layer is applied at the top of the domain from 16.3km.

The surface is assumed to be a tropical ocean with the temperature set at 300K. In order to keep the boundary conditions as simple as possible for the initial investigation, there is no imposed convergence into the domain, no forced uplift, no imposed wind shear and no rotation. The model run lasted 50 days, initialised from the final state of a previous simulation that had a fixed imposed radiative forcing. The initial conditions should however be unimportant since an equilibrium regime is achieved which is independent of the initial state.

3 EQUILIBRIUM STATE

In this section a few characteristics of the initial equilibrium state will be described.

The approach to equilibrium is charted in Figure 2 which shows timeseries of the domain averaged temperature, water vapour (q_v) mass per unit column, and convective available potential energy (CAPE). The CAPE value is calculated using the bottom model level (40m) as the starting point of the parcel accent.

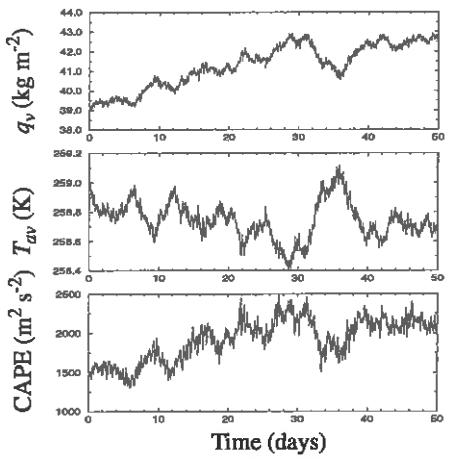

Figure 2. Timeseries of domain averaged temperature, column water vapour and CAPE for the first 50 days of integration. Data-points are on average 4.5 minutes apart. The data is unsmoothed.

When exponential curves are fitted to the data the time-constant for the approach to equilibrium is around 20 to 25 days, of similar order to the adjustment timescales of both the earlier 2D investigations of L93 and H93. The adjustment timescale is however longer than that of L93, perhaps because of the absence of imposed convergence which acts as an additional forcing, although the different dynamics could also play a role. In comparison, the 3D experiments of Robe and Emanual (1995) and Islam et al. (1993) with fixed radiative forcing and simple microphysics reported a shorter equilibrium adjustment timescales of the order of a few days.

In addition to this long timescale shorter timescales are also in evidence. Firstly oscillations of the period of hours associated with the cumulus timescale are apparent in all three time series. There is also a longer timescale on the order of 5 days or so, which could possibly be associated with a 'cumulus cluster' timescale. One result that is perhaps surprising is that CAPE evolves on the same slow 25 day timescale as q_v. There is also remarkable correlation between q_v, T_{av} and CAPE on all timescales.

It is clear from these plots that equilibrium has been reached by day 40 of the experiment. If the quantities are averaged between day 40 and 50, then the equilibrium state has an domain average temperature of 258.7K, water vapour content of 42.5 kg m^{-2}, and a CAPE value of 2100 m^2 s^{-2}.

These values can be compared to the control run of L93 that utilised a surface temperature of 301K, one degree warmer. The domain averaged temperature is very similar to the 257.6K of L93. On the other hand the equilibrium atmosphere of L93 is substantially moister. The q_v content at the lowest model-level is approximately 17g kg^{-1} in both experiments, equivalent to a RH value of approximately 80%. However, both H93 and L93 use the bulk aerodynamic formulae to specify surface fluxes, with an arbitrarily imposed minimum surface wind-speed. The specification of this wind-speed has a large influence on the boundary layer dry entropy and RH (in addition to any fixed imposed convergence of heat and moisture into the domain), and this should be considered when comparisons are made. In L93 the surface fluxes of q_v, representing 24% of the moisture source, had an equilibrium value of 4.2 kg m^{-2} day^{-1}. Linear interpolation between the two experiments of H93 gives a q_v flux of 3.1 kg m^{-2} day^{-1} for a surface temperature of 300K. In this 3D experiment the surface flux of q_v (in this case the only moisture source) is 4.6 kg m^{-2} day^{-1} in the equilibrium state, balanced of course by surface precipitation.

To examine the vertical structure of the equilibrium atmosphere a tephigram of the domain averaged temperature and vapour profiles for the last 10 days of integration is shown in Figure 3. There are several characteristics worthy of comment.

- It can be seen that the model has a resolved boundary layer that is dry-adiabatic and almost constant in q_v. This resolved boundary layer appears to be approximately 450m in depth. This characteristic was absent from the q_v profiles of L93 and H93.
- The temperature profile is roughly moist adiabatic, although conditional instability is in evidence.
- From the enhanced values of q_v in the 200 to 250mb layer it would seem that the majority of deep convective clouds detrain at this level. This is below the tropopause situated at the 100mb level.

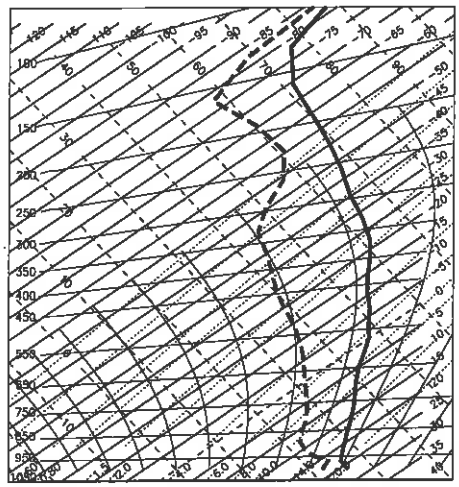

Figure 3. Tephigram of the average sounding between day 40 and 50 of the integration.

4. CONCLUSIONS

A three dimensional cloud resolving model, with a fully interactive radiation scheme for both the IR and SW spectrums, and a three phase microphysical scheme, has been configured to model a simple tropical scenario, and has been operated to a state of statistical radiative-convective equilibrium. The model and the experimental setup have been briefly described, and time series' plotted to illustrate that equilibrium status has indeed been achieved. The e-folding time-constant for the adjustment to equilibrium appears to be on the order of 20-25 days.

When compared to the previous study of L93 the temperature profiles of the two equilibrium states are very similar with the tropopause occurring at the same level and temperature, and a similar domain average temperature. However there are differences in the water vapour profile: The 3D equilibrium reported here has a boundary layer well-mixed in q_v and significantly lower midtropospheric values when compared to the control run of L93.

Future work will include experiments to examine the sensitivity of the equilibrium state to surface temperature perturbations, and an investigation into the origin of the long adjustment timescale for *all* model quantities.

The timescale for mixing water vapour through the troposphere at radiatively-determined subsidence rates is around 20-25 days. But why should q_v adjustment influence the timescale of CAPE? One hypothesis to be examined is that the q_v subsidence from clear-air regions has a significant impact on the boundary layer (B.L) moist-entropy budget, and that the B.L budget is key in determining convective activity, and therefore atmospheric thermodynamic properties and CAPE. The situation is complex since a source for q_v in the free-atmosphere is convective detrainment, and could be further complicated by the alteration of the radiatively determined environmental subsidence rate as a result of increased/decreased q_v

Raymond (1995) examined the tropical atmosphere in terms of a B.L "quasi"-equilibrium and concluded that the B.L timescale was largely determined by a balance of surface fluxes and convective down-draughts, resulting in a timescale on the order of 1/2 day. The B.L timescales are apparent in Figure 4 which shows water vapour at the bottom model level. Although the 1/2 day adjustment timescale is not insignificant, the longer timescale is also very evident. The existence of a longer timescale in B.L adjustment has also been suggested by Emanual et al. (1994). .

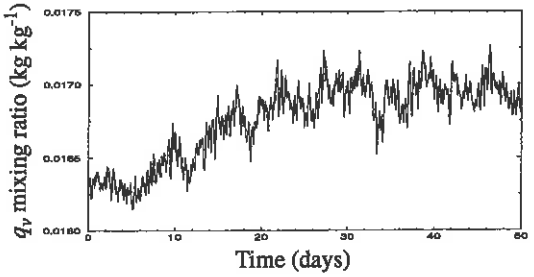

Figure 4. Mass mixing ratio of water vapour at the bottom model level (40m).

5. REFERENCES

Edwards, J. M., and A. Slingo, 1996: Studies with a flexible new radiation code. I: Choosing a configuration for a large scale model. *Q. J. R. Meteorol. Soc. in Press.*

Emanual, K. A., J. D. Neelin, and C. S. Bretherton, 1994: On large-scale circulations in convecting atmospheres. *Q. J. R. Meteorol. Soc.* **120**, 1111-1143.

Held, I. M., R. S. Hemler, and V. Ramaswamy, 1993: Radiative-Convective Equilibrium with Explicit Two-Dimensional Moist Convection. *J. Atmos. Sci.*, **50**, 3909-3927.

Islam, S., R. L. Bras, and K. A. Emanual, 1993: Predictability of mesoscale rainfall in the tropics. *J. Appl. Meteor.*, **32**, 297-310.

Lau, K. M., C. H. Sui, and W. K. Tao, 1993: A preliminary study of the tropical water cycle and its sensitivity to surface warming. *Bull. Amer. Meteor. Soc.*, **74**, 1313-1321.

Petch, J., 1995: Modelling the interaction of clouds and radiation using bulk microphysical schemes. PhD Thesis. University of Reading.

Raymond, D. J., 1995: Regulation of moist convection over the west Pacific warm pool. *J. Atmos. Sci.* **52**, 3945-3959.

Robe, F. R., and K. A. Emanual, 1995: Dependence of tropical convection on radiative forcing. *J. Atmos. Sci. Submitted.*

Shutts, G. J., and M. E. B. Gray, 1994: A numerical modelling study of the geostrophic adjustment following deep convection. *Q. J. R. Meteorol. Soc.* **120**, 1145-1178.

Swann, H., 1994: Cloud microphysical processes - a description of the parameterization used in the Large Eddy Model. *UK Meteorological Office, JCMM Internal Report No. 10.*

P7A.17

NUMERICAL EXPERIMENTS ON THE TROPICAL CYCLONE EYE

S. L. Gray* and G. C. Craig

Joint Centre for Mesoscale Meteorology, University of Reading,

1. INTRODUCTION

One of the most fascinating facets of relatively intense tropical cyclones is the existence of a warm central core, often free of clouds, in which the windspeeds are comparatively small; the tropical cyclone eye. Similar features are also observed in a group of highly convective polar lows that closely resemble tropical cyclones in structure. This work is motivated by the need to understand these features; the factors controlling the eye structure, dynamics and size. The eventual aim is to determine the minimal physics necessary to incorporate a realistic eye in a simple analytic or numerical balanced model.

The methodology is to use a primitive equation model to determine the sensitivity of the eye to various chosen parameters which could vary in nature and can be predicted to possibly affect eye development.

2. NUMERICAL MODEL

Experiments were carried out using a nonhydrostatic, axisymmetric model with convection treated explicitly, rather than parameterized. Both tropical cyclones (Craig, 1995) and polar lows (Craig, 1996) have been successfully simulated using this model.

The high horizontal resolution (5 km) used in the model provides, at least, tolerable resolution of the region within the radius of maximum windspeed.

3. EYE STRUCTURE

In both the tropical cyclone and polar low simulations the azimuthal velocities decay with height (as expected). Figure 1 shows that the radial structure of the boundary layer azimuthal velocity, v, inside the radius of maximum v, (r_{max}) is very different in the two simulations. The tropical cyclone eye region is in approximate solid body rotation i.e. $v \sim (r/r_{max})\, v_{max}$ with $r_{max} \sim 20$ km for the steady state system. This type of eye structure can only be maintained, in the presence of low-level radial outflow, through large eddy fluxes of angular momentum from the eyewall into the eye region which reach the central axis. This is consistent with observations (e.g. Marks et al., 1992).

The polar low eye region is not in solid body rotation and r_{max} is much greater than that observed in the tropical cyclone model at ~ 60 km for the steady state system. The azimuthal velocity inside the eyewall decays from that of the imposed initial vortex over time. The mature eye region is very calm with small v values outwards from the center to the eyewall where a sharp transition occurs to the high windspeed eyewall. Just inside the eyewall there is a small region where diffusional effects 'smear' out the velocity profile. The width of this transition region increases with height (not shown). There is some observational data which points to the possibility of polar lows with large, very calm eyes (Rasmussen et al., 1992).

A significant, positive temperature anomaly which peaks at two altitudes develops in both simulations and the heights and magnitudes of these peaks in the tropical cyclone simulation agree well with those in observed systems. The development of the radial thermodynamic structure in both versions of the numerical model is illustrated in Figure 2 which shows mean midlevel potential temperature. It can be seen that, although substantial warming occurs in the eye region in both versions of the numerical model as the system intensifies, only in the tropical cyclone model does the eye region warm more than the eyewall. The potential temperature structure is in approximate thermal wind balance with the azimuthal wind structure in both types of eye.

4. EYE DYNAMICS

It is generally agreed that the relatively high temperatures observed in the eye region of tropical cyclones, especially in the middle and upper troposphere, are a result of dry adiabatic warming through subsidence in a statically stable atmosphere.

Why does the eye warming exceed the eyewall warm-

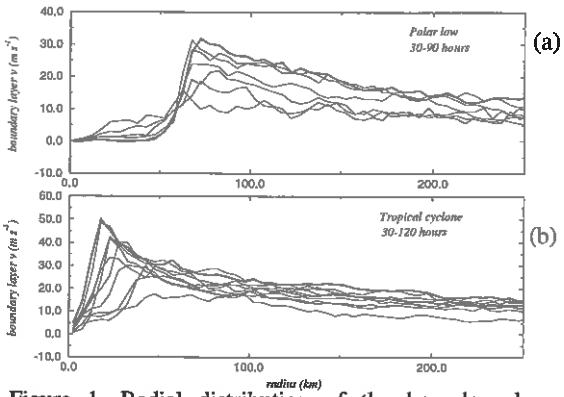

Figure 1. Radial distribution of the boundary layer azimuthal velocity at 10 hourly intervals for the a) polar low and b) tropical cyclone simulations. The last time plotted is in bold.

* *Corresponding author address*: Suzanne L. Gray, Department of Meteorology, University of Reading, 2 Earley Gate, Whiteknights, Reading, Berkshire, United Kingdom, RG6 2AU; e-mail S.L.Gray@rdg.ac.uk

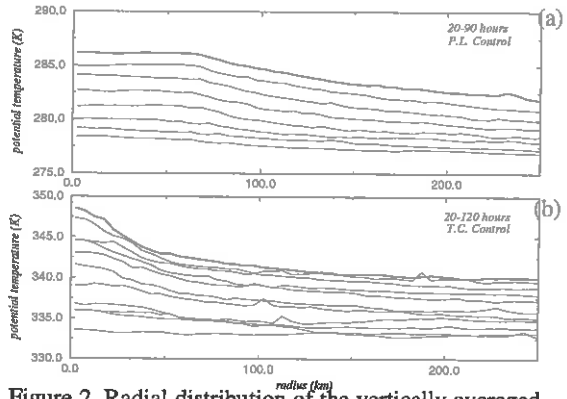

Figure 2. Radial distribution of the vertically averaged midlevel potential temperature at 10 hourly intervals for the a) polar low and b) tropical cyclone simulations. The last time is plotted in bold.

ing in the tropical cyclone but not the polar low simulations? There are two obvious possible causes: Firstly a lack of subsidence in the polar low eye and secondly a lack of warming through this subsidence. Ten hour averages of the radial mean vertical velocity (not shown) indicate that midlevel subsidence is occurring at approximately the same rate in both types of strongly intensifying vortex (peaking at ~ -0.04 m s^{-1}).

The initial vertical structure of potential temperature, θ, is shown in Figure 3. Both atmospheres are in a state which is approximately conditionally neutral to convection i.e. the equivalent potential temperature is approximately constant with height. The difference between the tropospheric θ profiles arises because in the high latitude, cold, relatively dry polar atmosphere, moist and dry adiabats become close to parallel and hence θ is also approximately constant with height. An almost statically neutral troposphere prevents the eye region from warming through the downwards advection of high θ air, unless air is transported across the tropopause. Hence, the potential temperature in the polar low eye cannot increase greatly for any reasonable rate of forced eye subsidence, and thus the eye cannot warm more than the eyewall. Thermal wind balance implies that no system developing in a similar arctic environment can have an eye in solid body rotation.

Various conditions must be satisfied to force sufficient subsidence warming to balance an eye in solid body rotation, even in a tropical environment. Horizontal diffusion of momentum was found to be essential in the system and the tropical cyclone simulations only developed eyes in solid body rotation when the eye radius was less than ~ 30 km.

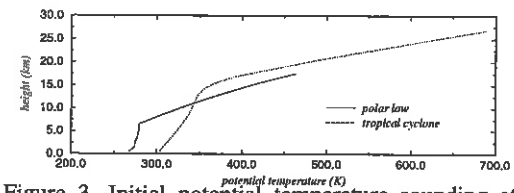

Figure 3. Initial potential temperature sounding at the center of the numerical model vortex (first radial grid point) after adjustment to thermal wind balance following insertion of the imposed initial vortex.

5. EYE SIZE

Intensification of tropical cyclone type vortices occurs when air is advected inwards at low-levels conserving (to some degree) absolute angular momentum. Factors affecting the momentum budget in the system may thus also affect the size and structure of the eye.

Simulations were performed using the numerical model to examine the sensitivity of the model eye to the absolute angular momentum of the imposed initial vortex (controlled by the Coriolis parameter and the radial distribution of v in the initial vortex), to surface friction and to the intensification rate of the vortex.

As an example of the results, Figure 4 illustrates the dependence on surface friction (varied through a nondimensional drag coefficient incorporated in the bulk aerodynamic formulae used in the model). Note that the eye size decreases with increasing surface friction and that in the case with zero surface friction the eye is not in solid body rotation. Increasing the intensification rate by increasing the heat fluxes from the sea surface (through the nondimensional heat and moisture transfer coefficients) increases the steady state eye size (not shown).

6. CONCLUSIONS

A significantly statically stable troposphere and horizontal momentum diffusion were found to be essential for the formation of an eye in solid body rotation in a numerical model. The mechanisms controlling the size of the eye require further study since no theories have been proposed which explain the above results.

7. REFERENCES

Craig, G. C., 1995: Radiation and polar lows. *Quart. J. Roy. Meteor. Soc.*, **121,** 79-94.

Craig, G. C., 1996: Numerical experiments on radiation and tropical cyclones. *Quart. J. Roy. Meteor. Soc.*, **122,** 415-422

Marks, F. D. Jr., R. A. Houze, Jr and J. F. Gamache, 1992: Dual-aircraft investigation of the inner core of hurricane Norbert. Part I: Kinematic structure. *J. Atmos. Sci.*, **49,** 919-942.

Rasmussen, E. A., T. S. Pedersen, L. T. Pedersen and J. Turner, 1992: Polar lows and arctic instability lows over the bear island region. *Tellus*, **44a,** 133-154.

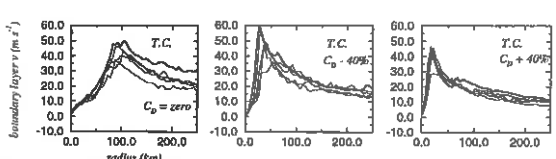

Figure 4. Radial distribution of boundary layer azimuthal velocity at 10 hourly intervals from 70 to 120 hours (tropical cyclone, T.C.) for runs with labeled deviations of the frictional drag coefficient, C_D, from the control value. The last time plotted is in bold.

P7A.18

EVOLUTION OF TROPICAL CYCLONE BOUNDARY LAYER

Chien-Liang Uang* and Chris Thorncroft

Department of Meteorology
University of Reading
U. K.

1. INTRODUCTION

Previous studies (for example, Malkus and Riehl 1960; Emanuel 1986; Holland 1995) have shown that the maximum potential intensity of tropical cyclones can be estimated from the boundary-layer moist entropy, as expressed by equivalent potential temperature, θe. The evolution of the boundary-layer θe is therefore crucial for the development of tropical cyclones. The sea surface heat fluxes are acting to increase the boundary-layer θe. On the other hand, descents bring down low-θe air as the main sink. The equilibrium boundary-layer θe is an important parameter for determining the development and intensity of tropical cyclones. In this study, it is aimed to study numerically the evolution of the tropical cyclone boundary layer θe and its impact on the development and intensity of the tropical cyclone.

From observations of two tropical storms, Korolev, Petrichenko, and Pudov (1990) found that the temperature difference between the sea and 10-m air increased with wind speeds. The air is cooler by about 1°K at wind speeds less than 20 ms^{-1} and linearly increased to 5-6°K at wind speeds of 26 ms^{-1}. The Bowen ratio, defined as the ratio of sensible heat flux to latent heat flux, also increased from 0.1 to 0.4 as the wind strengthened. They hypothesised that the sharp cooling of the near-water atmosphere was due to the absorption of heat for the evaporation of sea spray. It is, therefore, desired to investigate if such cooling is due to the evaporation of sea spray. Furthermore, Lighthill et al. (1994) suggested that the intensifying tropical cyclone may have a self-limiting character because intense winds at the sea surface receive their energy input at a temperature significantly depressed by evaporation of spray. Here, we would like to investigate the effects of sea spray on tropical cyclones.

* *Corresponding author address*: Chien-Liang Uang, Dept. of Meteorology, Univ. of Reading, Reading, U.K.;e-mail <c.l.uang@reading.ac.uk>.

2. NUMERICAL MODEL

The numerical model used in this study is a modified version of that developed by Rotunno and Emanuel (1987). It is a nonhydrostatic, axisymmetric model with convection explicitly accounted for. The prognostic equations are integrated on an *f*-plane for momentum, potential temperature, nondimensional pressure and mixing ratios of water vapour, cloud water, rain and ice. Note that only water vapour and liquid water were considered in Rotunno and Emanuel (1987).

To better represent the boundary layer, the vertical coordinate has been modified to have the lowest level at 10 m, a constant resolution of 50 m in the lowest 500 m and stretched grid spaces upwards. The vertical domain remains at 25 km with a sponge layer at the top. The turbulence parametrization is retained to be a first-order Richardson number-dependent eddy viscosity. The mixing length, l, is proportional to the grid-spacing, Δz: $l=0.23\times\Delta z$. From the sea surface, the momentum flux and 'direct' sensible and latent heat fluxes are estimated by bulk aerodynamic formulae. The momentum drag coefficient, C_D is given by Deacon's formula, $C_D=1.1\times10^{-3}+4\times10^{-5}V_{10}$, where V_{10} is the 10-m horizontal wind. The transfer coefficients for both sensible and latent heat fluxes are set to 1.2×10^{-3}.

In addition to the direct heat fluxes, the wind-generated spray transfers sensible (Q_S) and latent (Q_L) heat to the air. While transferring latent heat through evaporation, an equivalent amount of sensible heat of the air is absorbed. Therefore, the total spray-mediated sensible heat flux is Q_S+Q_L. In the model, the parametrization of sea spray-mediated heat fluxes, developed by Fairall, Kepert, and Holland (1994), has been incorporated. In the parametrization, the spray-mediated heat fluxes are determined by the sea surface temperature and the

10-m humidity, temperature, and wind speed. The implementation of this parametrization in the numerical model gives additional fluxes from the sea surface to 10-m air. Using H_S and H_L to denote the direct sensible and latent heat fluxes, respectively, the total heat fluxes are then given by

Sensible Heat: $H_S+Q_S-Q_L$

Latent Heat: H_L+Q_L.

In the subcloud layer, the evaporation of raindrops also plays an important role in determining the thermodynamic structure of the layer (e.g., Betts and Simpson 1987). Both the evaporation and melting cooling are important in regard to generating downdraughts (Srivastava 1987). To estimate these microphysical processes more accurately, the microphysical scheme of Ferris (1989), operationally used by the U. K. Meteorological Office, is utilised in the model. In that scheme, four categories of water: water vapour, cloud water, rain, and ice, are considered.

In all experiments shown here, the environment is prescribed using the mean hurricane season sounding of Jordan (1958) with sea surface pressure of 1015.1 hPa and sea surface temperature of 26.3°C. The initial vortex, as specified in Rotunno and Emanuel (1987), has the maximum tangential wind of 12 ms^{-1} at radius of 82.5 km and the outer edge at radius of 412.5 km. The Coriolis parameter is evaluated at 15 °N.

3. RESULTS AND DISCUSSION

3.1 sea-spray impacts on tropical cyclone's intensity

Results of three experiments, designed to test the tropical cyclone's sensitivity to sea spray, are presented here. Exp. c15 is the control run without sea spray. Exp. shd is identical to Exp. c15 in the first 100 hours of integration. Afterwards, the sea spray-mediated fluxes take place. The third one, Exp. spr, includes sea spray-mediated fluxes from the very beginning of integration. All three experiments have been run for 250 hours.

Figure 1 shows the time series of one-hour averaged minimum pressure of all three experiments. Note that the curves have been smoothed. From the time series, it is indicated that after about 180 hours of integration the average of the maximum intensities of cyclones in three experiments are similar to each other. Exps. c15 and shd even evolve in a rather close pattern. Inspecting the average field of tangential winds of the model cyclones (not shown here), there is no significant difference in cyclones' intensity between Exps. c15 and shd after 180 hours of integration. In contrast, Exp. spr has a slightly less intense cyclone. It is therefore suggested that the maximum intensity of tropical cyclones is not substantially affected by the sea spray. Close examination shows no significant difference in the boundary-layer θe in the experiments consistent with this result. However, the detail of the cyclone's evolution varies among the three experiments as shown in the time series before reaching their maximum intensity.

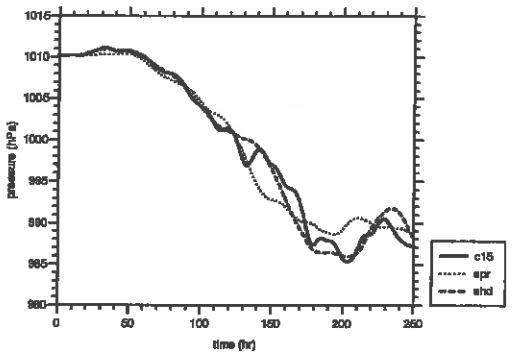

Figure 1. Time series of minimum pressure of experiments c15, spr and shd.

3.2 cooling of atmosphere near sea surface

Figure 2 shows the dependence of sea-air temperature difference and Bowen ratio on wind speeds sampled from Exps. c15 and spr after 100 hours of integration. Both experiments indicate that both the sea-air temperature difference and Bowen ratio increase with wind speeds, though the distribution of two parameters against wind speeds is more scattered without sea spray. Note that the increase of Bowen ratio with wind speeds is in agreement with observations mentioned earlier. The temperature difference shown here does not increase with wind speeds as sharp as observed. However, in other experiments with SST=31.3°C, the sea-air temperature difference increases with wind speeds in a manner like the observations.

Whatever mechanism makes cooling increase with wind speeds must also decrease the sea-air humidity contrast in order to increase the Bowen ratio. It is hypothesised here that the increase of cooling with wind speeds is a result from the evaporation of not only sea spray, but also raindrops. Since the cooling due to evaporation of raindrops does not necessarily coexist with strong winds, this may be the reason why the distribution of temperature difference is more scattered in Exp. c15.

Since the evaporation of sea spray has strong dependence on wind speeds, it can make the correlation between cooling and Bowen ratio and wind speeds higher, as shown in Exp. spr and is more consistent with observations.

4. SUMMARY

The results of this study illustrate that the development of a tropical cyclone is modified by the presence of sea spray, though its maximum intensity is not substantially affected. It is suggested that the sea spray has to be included to better simulate the evolution of tropical cyclones. Further study is currently carried out to reveal how the sea spray works to affect the development of tropical cyclones.

Another important process to modify the boundary-layer θe is the downward flux of low-θe air. Using the model described here, the effect of descents on the boundary-layer θe has been studied. The model has also been coupled with an ocean model to further simulate the evolution of tropical cyclones including the effect of the wind-induced cooling of the sea water. In the coupled model study, the effect of the sea spray will also be examined. Results will be shown in the conference.

5. REFERENCES

Betts, A.K., and J. Simpson, 1987: Thermodynamic budget diagrams for the hurricane subcloud layer. J. Atmos. Sci., 44, 842-849.

Emanuel, K. A., 1986: An air-sea interaction theory for tropical cyclones. Part I: Steady state maintenance. J. Atmos. Sci., 43, 585-604.

Fairall, C.W., J.D. Kepert and G.J. Holland, 1994: The effect of sea spray on surface energy transports over the ocean. The Global Atmosphere and Ocean System. 2, 121-142.

Ferris, P., 1989: A proposed Mixed Phase Precipitation scheme for the mesoscale model. U.K. Meterological Office Working Paper No. 114.

Holland, G.J., 1995: The maximum potential intensity of tropical cyclones. J. Atmos. Sci. (submitted)

Jordan, C.L., 1958: Mean soundings for the West Indies area. J. Meteor., 15, 91-97.

Korolev, V.S., S.A. Petrichenko, and V.D. Pudov, 1990: Heat and moisture exchange between the ocean and atmosphere in tropical storms Tess and Skip. Meteorologiya i Gidrologiya, 2, 108-111.

Lighthill, J., G. Holland, W. Gray, C. Landsea, G. Craig, J. Evans, Y. Kurihara, And C. Guard, 1994: Global climate change and tropical cyclones. Bull. Amer. Meteor. Soc., 75, 2147-2157.

Malkus, J. S., and H. Riehl, 1960: On the dynamics and energy transformations in steady state hurricanes. Tellus, 12, 1-20.

Rotunno, R. and K.A. Emanuel, 1987: An air-sea interaction theory for tropical cyclones. Part II: Evolutionary study using a nonhydrostatic axisymmetric numerical model. J. Atoms. Sci., 44, 542-561.

Srivastava, R. C., 1987: A model of intense downdraughts driven by the melting and evaporation of precipitation. J. Atmos. Sci., 44, 1752-1773.

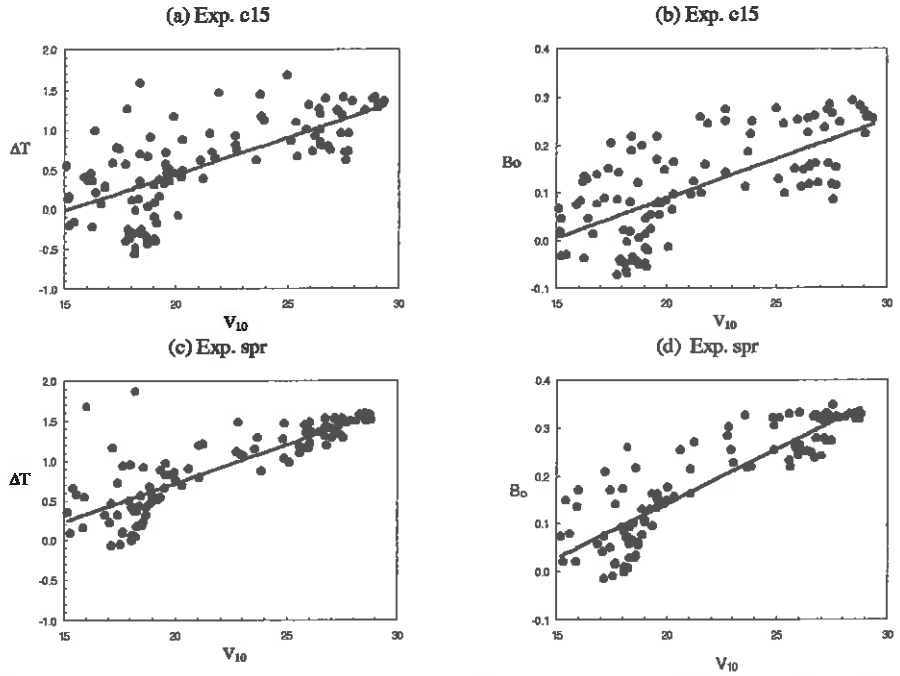

Figure 2. (a) and (b) show respectively the dependence of the sea-air temperature difference (in °C) and Bowen ratio on wind speed (in ms^{-1}) for Exp. c15. (c) and (d) are as (a) and (b) but for Exp. spr.

P7B.3 LEE VORTICES DUE TO FLOW PAST MESOSCALE MOUNTAINS

Jorge Gutiérrez* and Alan J. Thorpe

JCMM, University of Reading, UK

1. INTRODUCTION

In the past few years meteorologists have looked at the mechanisms that generate vorticity when stratified flow interacts with an obstacle. An important contribution to the field came from Smolarkiewicz and Rotunno (1989) who showed that lee vortices can be generated in the absence of frictional processes. Sun and Chern (1994) observed that these inviscid vortices can be shed when some asymmetries are introduced in the upstream flow. Smith (1989) objected to Smolarkiewicz and Rotunno's claim that no potential vorticity had been produced in their simulations. There can be a continuous production of potential vorticity due to the internal dissipation of the numerical model or, after a period where no potential vorticity has been created, a sudden production of potential vorticity starts taking place as soon as hydraulic jumps appear in the flow thus creating the vorticity that gives rise to the two counter-rotating lee eddies observed in Smolarkiewicz and Rotunno's simulations.

The problem of the evolution of the potential vorticity field in inviscid numerical simulations remains an open question, and is considered here.

Another question of interest deals with the relative importance of the baroclinic source of vorticity as compared with frictional sources of vorticity in the case of a low Froude number viscous flow interacting with orography. This is an important subject of research since frictional processes are always present in the real atmosphere.

Another goal of this research is the determination of the areas where potential vorticity is produced when viscous low Froude number flow interacts with orography.

* *Corresponding author address*: Jorge Gutiérrez, Dept. of Meteorology, University of Reading, Reading RG6 2AU, UK; e–mail <swrgutie@reading.ac.uk>.

2. EXPERIMENTAL SET-UP

The simulations presented here correspond to westerly flow of air through a region containing an isolated bell-shaped mountain with a circular base. The height of the mountain is 2 Km and its radius is 50 Km. The background flow has a speed of 4 ms^{-1} and in inviscid simulations it has no shear and a free-slip lower boundary condition is applied. The Brunt-Väisälä frequency has a constant upstream value of $10^{-2}s^{-1}$, thus the Froude number ($Fr = \frac{U}{Nh}$) is 0.2.

In simulations of viscous flow a no-slip lower boundary condition has been used and a simple boundary layer with a constant eddy viscosity coefficient of 5 m^2s^{-1} has been implemented.

All the numerical simulations have been made with a three-dimensional, sigma coordinate, non-linear, non-hydrostatic model developed at the University of Reading; Miranda and James (1992).

3. EVOLUTION OF THE VORTICITY AND THE POTENTIAL VORTICITY FIELDS

3.1 *Inviscid flow*

Consider a westerly flow impinging on the mountain without background rotation. Return flow is observed after 4 hours of simulation at a height of 400 metres over level terrain. A total integration of twelve hours yields two well defined counter-rotating vortices on the lee of the mountain. Two areas of vertical vorticity are found on the lee of the orography, the one located on the northern part of the lee contains anticyclonic vorticity and the one located at the south of the vortex has cyclonic vorticity. An area of negative potential vorticity is found on the northern part of the wake and an area of positive potential vorticity is found on the southern part of the wake. The

vorticity decreases with height. In order to see if the potential vorticity is generated before or after the vortices are fully grown an investigation of the evolution of the potential vorticity field has been done. To trace the evolution of the vorticity field together with that of the potential vorticity field, consider a 'normalised ' potential vorticity defined as:

$$PV_{norm} = \frac{\rho PV}{\frac{\partial \theta_{back}}{\partial z}} \qquad (1)$$

Notice that PV_{norm} has units of vorticity. The extrema of PV_{norm} and vorticity on the northern vortex at each hour for a period of eight hours are given in figure 1 showing that PV_{norm} and vorticity are created since the early stages of the integration. This is an indication that some viscous process is taking place and that it occurs since the early moments of the integration. Examination of several vertical sections of the isentropes does not lead one to think that a hydraulic jump is present. Thus, the existence of this PV_{norm} can be attributed to the implicit diffusion of the numerical model. In the model, spatial filtering has been applied in order to avoid the build up of two grid length waves, which could lead to the onset of non-linear instability. A fourth-order smoothing is applied on the model surfaces and on the perturbation wind.

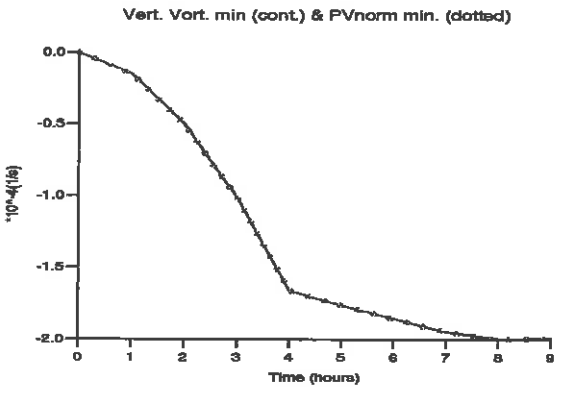

Figure 1: Evolution of vorticity and PV_{norm}

The main source of horizontal vorticity is the baroclinic term, therefore, as explained by Smolarkiewicz and Rotunno (1989), the deformation of the isentropes produces horizontal vortex tubes that are tilted in the vertical as the flow moves around the orography producing in this way vertical vorticity that will give rise to the vortices that are formed on the lee of the mountain.

The introduction of background rotation breaks the symmetry of the upstream flow and induces the shedding of eddies. An analysis of the vorticity budget shows that the baroclinic term is the main generator of horizontal vorticity. The horizontal structure of the vorticity field varies greatly with respect to that obtained for the same field without background rotation. An area of positive vorticity is found on the upstream slope of the mountain closely followed as the orography is approached by a negative area of vorticity. This is caused by stretching of the vortex tubes due to separation of the isentropes as the flow approaches the mountain followed by a contraction of the vortex tubes due to the compression of isentropes as the flow begins to move up the slope of the orography.

3.2 *Viscous flow*

The simulations of viscous flow show that the maximum of vorticity is located on the lee slope of the mountain, but this zone 'rotates' with height inside the boundary layer. For a westerly flow in the northern hemisphere, negative potential vorticity is found on the northern flank of the orography and positive potential vorticity is located on the southern flank. This result confirms the prediction of Thorpe et al. (1993) who explained that as the orography slopes upward the boundary layer is tilted such that it acquires a slope producing a horizontal velocity gradient that contributes to anticyclonic potential vorticity, to the north of the orography and the opposite to the south. An analysis of the different terms of the vorticity equation shows that the horizontal vorticity produced by the baroclinic term is ten times smaller than that produced by tilting terms associated to viscous processes. This result shows that the baroclinic term, at least in the case of a simple boundary layer parametrisation, is negligible compared to other vorticity production terms.

4. CONCLUSIONS

It has been found that in inviscid simulations with a free slip lower boundary condition and no background rotation PV_{norm} is produced since the early stages of the simulation. This is attributed to the internal diffusion of the model since no evidence of hydraulic jumps has been found for flow with a Foude number of 0.2. The existence of lee vortices is thus attributed to the tilting of horizontal vorticity that has been produced by the deformation of the isentropes as the flow moves around and over the orography. The introduction of background rotation in inviscid simulations breaks the upstream symmetry of the flow and induces vortex shedding. An analysis of the vorticity budget shows that the baroclinic term is the main source of horizontal vorticity. When viscous processes are introduced two main areas of PV_{norm} production are found to be located at the flanks of the orography. In this regime the baroclinic term is much smaller than other vorticity production terms, indicating that perhaps it may not play an important role in the real atmosphere.

5. REFERENCES

Miranda, P. and James I. N., 1992: Non-linear three-dimensional effects on gravity-wave drag: splitting flow and breaking waves. *Quart. J. Roy. Meteor. Soc.*, **118**, 1057-1081.

Smith, R., 1989: Comment on 'Low Froude number flow past three-dimensional obstacles. Part I: Baroclinically Generated Lee Vortices'.*J. Atmos. Sci.*, **46**, 3611-3613.

Smolarkiewicz and R. Rotunno, 1989: Low Froude number flow past three dimensional obstacles. Part I: Baroclinically generated lee vortices. *J. Atmos. Sci.*, **46**, 1154-1164.

Sun, W. and J. Chern, 1994: Numerical experiments of vortices in the wakes of large idealized mountains. *J. Atmos. Sci.*, **51**, 191-209.

Thorpe, A. J., Volkert, H. and Heimann, D., 1993: Potential vorticity of flow over the Alps. *J. Atmos. Sci.*, **50**, 1573-1590.

P7B.14 RICHARDSON NUMBER VARIATION OF STABLE BOUNDARY LAYER FLOW OVER HILLS

J. J. Holden*, S. E. Belcher, S. H. Derbyshire

University of Reading
Reading, England

1 INTRODUCTION

Although extensive research has been carried out for stable boundary layer flow over flat terrain (e.g. Derbyshire, 1990), relatively little is known about stably stratified flow over hills. Nappo (1991) observes that sporadic breakdown events are a regular feature of the stable nocturnal boundary layer over flat terrain and suggests that these events may be influenced by nearby hills. There are many other phenomena observed in stable boundary layer flow over hills which are not well understood, such as the idea of flow decoupling and drainage currents. Understanding these processes is crucial to the correct parameterisation of small scale orography in NWP models (Wood and Mason, 1991). Belcher & Wood (1995) develop a model for weakly stratified flow over hills but this cannot be applied to strong stratification.

We consider stably stratified boundary layer flow over hilly terrain by developing a linear model and relating the results to experimental observations made by MRU Cardington in the Llanthony Valley, Wales (1994).

2 ANALYSIS OF LINEAR PERTURBATIONS TO FLOW

When the atmospheric boundary layer flows over undulating terrain the stability of the flow can change. This change can be characterised by the gradient Richardson number, Ri, which is defined as:

$$Ri = \frac{N^2}{S^2}, \tag{1}$$

where N is the buoyancy frequency and $S = \partial u/\partial z$ is the vertical wind shear. A flow is statically stable when Ri is positive but can become dynamically unstable as Ri becomes small. The value of Ri at which the air becomes dynamically unstable is referred to as the *critical* Richardson number, Ri_c. Linear analysis suggests that $Ri_c = \frac{1}{4}$. This criterion will be used to determine the dynamical stability of different regions of flow over undulating terrain.

Following Miles (1993) it is appropriate to use a streamline coordinate system to analyse changes to the mean flow induced by the hill. We define the coordinates:

$$\begin{aligned} \eta &= z - h(\xi, \eta) \\ \xi &= x, \end{aligned} \tag{2}$$

where $h(\xi, \eta)$ is the vertical displacement of a streamline from its mean position and $h = h_s(\xi)$ at the surface $\eta = 0$ (Fig. 1). The steady base flow is defined to have a linear velocity profile, $U_0(\eta)$ and a linear density profile, $\rho_s + \rho_0(\eta)$ where ρ_s is the density of air at the surface. The flow is then perturbed by a sequence of two-dimensional ridges, the surface of which is defined by $z = h_s(x)$. The wavelength, λ, of the hills is assumed to be much greater than their amplitude, a, such that $a/\lambda \ll 1$. By considering the linear perturbations to the flow, the linearised, two-dimensional momentum and continuity equations can be combined to form a differential equation for $\hat{h}(\eta)$ where $h(\xi, \eta) = \hat{h}(\eta)e^{ik\xi}$:

$$\begin{aligned} \frac{d^2\hat{h}}{d\eta^2} + \left\{ \frac{2}{U_0}\frac{dU_0}{d\eta} - \frac{(N^2)_0}{g} \right\} \frac{d\hat{h}}{d\eta} \\ + \left\{ \frac{(N^2)_0}{U_0^2} - k^2 \right\} \hat{h} = 0, \end{aligned} \tag{3}$$

with boundary conditions imposed at the surface and the top of the boundary layer, H,

* *Corresponding author address*: John J. Holden, University of Reading, Dept. of Meteorology, Reading, UK. RG6 2AU; e-mail <J.J.Holden@rdg.ac.uk>.

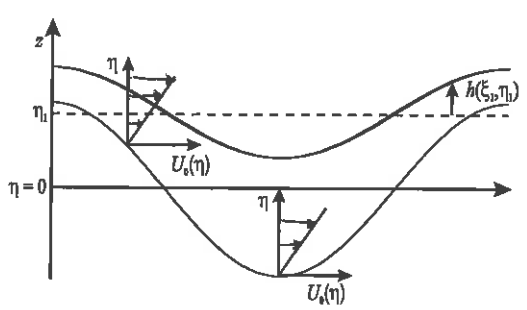

Figure 1 A diagram of the streamline coordinate system. $h(\xi, \eta)$ is the vertical displacement of a streamline from its unperturbed position.

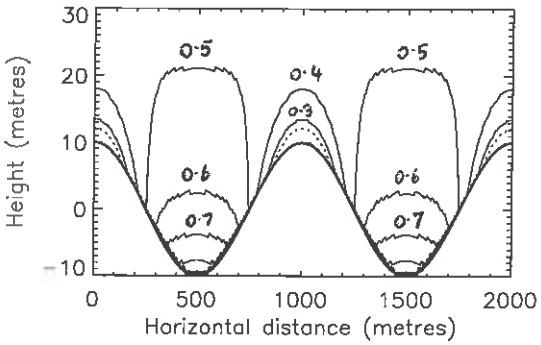

Figure 2 A plot showing the Richardson number contours for a base flow of $Ri_0 = \frac{1}{2}$ perturbed by a ridge-valley system with a surface described by $h_s = Re\{ae^{ik\xi}\}$. The dotted line represents $Ri_0 = \frac{1}{4}$.

$$\hat{h}(\eta = 0) = a$$
$$\hat{h}(\eta = H) = 0. \qquad (4)$$

Equation 3 can be solved numerically to find a solution for $\hat{h}$ from which other quantities including the Richardson number can be derived. Figure 2 shows contours of Ri plotted for the ridge-valley system of wavelength 1000 m, with $Ri_0 = \frac{1}{2}$. We use a wind shear, $S_0 = 0.05\,\mathrm{s}^{-1}$, and a vertical density gradient, $\partial\rho_0/\partial z = -1.5 \times 10^{-4}\,\mathrm{kg\,m}^{-4}$, with a surface density, $\rho_s = 1.2\,\mathrm{kg\,m}^{-3}$.

The reduction in Ri above the crest of the hill indicates a reduction in dynamical stability in this region. Also in this case Ri falls below the critical value of $\frac{1}{4}$ near the surface of the crest implying that the flow is no longer stable to small perturbations and we expect turbulence to develop in this region. This could be a possible generation mechanism for the the outbursts of sporadic turbulence which have been observed in nocturnal boundary layers (e.g. Nappo, 1991). Further work will address this question. In the valley, the Richardson number has increased suggesting an increase in dynamical stability.

3 COMPARISON WITH OBSERVATIONAL DATA

Observations have been made of the nocturnal boundary layer by MRU Cardington in the Llanthony Valley, Wales. Measurements were made using a tethered-balloon system described by Lapworth and Mason (1988). The helium-filled kite balloon is attached to a thin tether cable with turbulence probes clamped at various heights to measure temperature, pressure, humidity and wind velocity.

Figure 3 shows a plot of windspeed as a function of height for early evening (when the boundary layer is relatively neutral) and late evening (when the boundary layer has become stably stratified) on the night of 1 November 1994. In the early evening the wind profile is typical of the surface layer increasing from zero at the surface and tending to a constant value of around $8\,\mathrm{m\,s}^{-1}$ aloft. However, in the late evening the windspeed tends to zero at around 150 m and then increases again to about $1\,\mathrm{m\,s}^{-1}$ near the surface. Figure 4 shows a plot of the wind direction with height. In the early evening, the wind direction is almost constant with height at about 270 degrees. In the late evening, the wind direction is constant above 300 m, then it turns through about 30 degrees as the surface is approached until at around 150 m there is a dramatic change in wind direction to 315 degrees at the surface which corresponds to the down-valley direction.

Very stable air suppresses turbulence by inhibiting vertical fluxes of heat and momentum. This can lead to the air becoming decoupled from a relatively less stable mean flow. Considering the results presented in Figs. 3 & 4 together, we

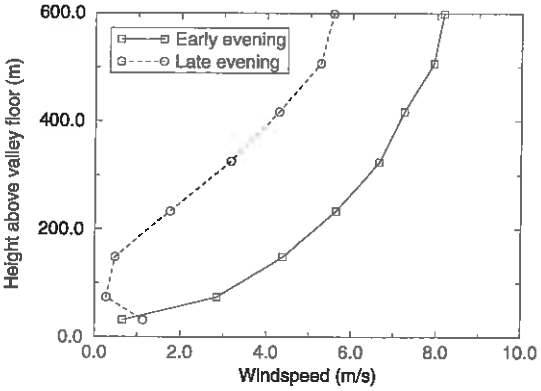

Figure 3 A plot showing windspeed above the valley floor as a function of height for early and late evening.

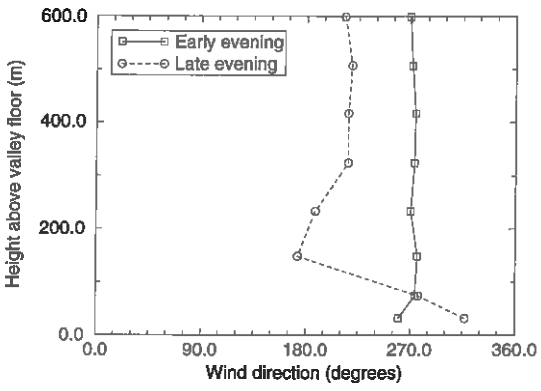

Figure 4 A plot showing wind direction above the valley floor as a function of height for early and late evening.

believe that the flow near the surface of the valley has become decoupled from the mean flow aloft and is flowing down the valley. This observational result is consistent with the calculation in §2 which predicted regions of high dynamical stability in the valley which would inhibit turbulence.

4 CONCLUDING REMARKS

We have established how the Richardson number varies for flow over hilly terrain. High dynamical stability was predicted in the valley which was supported by observational data. Further understanding of the dynamics might offer an explanation for the decoupling phenomena. This could have serious implications for NWP models which rely on parameterisation of small scale orography by roughness lengths. A valley containing air decoupled from the mean flow will have its roughness length reduced.

The dynamical stability was found to decrease above the crest of the hill and we expect turbulence to be generated in this region. Further work will consider the effect of Richardson number variation on turbulence generation and the feedback on the local Richardson number which might lead to an understanding of sporadic breakdown events.

5 REFERENCES

Belcher, S.E., and N. Wood, 1995: The form and wave drag due to stably stratified turbulent flow over low ridges. *To appear in Q J R Meteorol. Soc.*

Derbyshire, S.H., 1995: Stable boundary layers: Observations, models and variability part I: Modelling and measurements. *Boundary-Layer Meteorol.*, **74**, 19-54

Lapworth, A.J., and P.J. Mason, 1988: The new Cardington balloon-borne turbulence probe system. *J. Atmos. Oceanic Technol.*, **5**, 699-714

Miles, J.W., 1993: Surface-wave generation revisited. *J. Fluid Mech.*, **256**, 427-441

Nappo, C.J., 1991: Sporadic breakdowns of stability in the PBL over simple and complex terrain. *Boundary-Layer Meteorol.*, **54**, 69-87

Wood, N., and P.J. Mason, 1991: The influence of static stability on the effective roughness lengths for momentum and heat transfer. *Q J R Meteorol. Soc.*, **117**, 1025-1056

P7B.26 OMEGA-EQUATION ATTRIBUTION APPLIED TO SEVERE WEATHER EVENTS IN THE WESTERN MEDITERRANEAN

Maria Athanassiadou* and Alan J. Thorpe

Department of Meteorology
University of Reading, UK

1. INTRODUCTION

The western Mediterranean is characterised by complex terrain and as a result it is prone to a variety of meteorological events on a broad range of scales, from synoptic to meso-gamma.

The ANOMALIA project is an EC project, whose main objective is to study severe weather events in the western Mediterranean area, with emphasis on cases that produce torrential rain and floods. The project is shared among four European Institutions (JCMM-Reading, FISBAT-Bologna, UIB-Palma de Mallorca and LA-Toulouse), and aims to provide a better understanding of the non-linear interaction processes taking place as a consequence of the close proximity of mountains and sea in the western Mediterranean region, particularly in those seasons (autumn, winter) in which the sea acts as a powerful source of latent and sensible heat.

Five representative case studies have been selected for study, each associated with a "typical" synoptic situation. These are: (a) *Libya case* (22-25 Nov., 1990), (b) *Menorca case* (7-11 Oct., 1992), (c) *Algeria case* (1-7 Feb., 1993), (d) *Brig case* (21-25 Sept., 1993) and (e) *Piedmont case* (3-7 Nov., 1994).

2. OMEGA EQUATION ATTRIBUTION

Large precipitation is linked with strong (local) ascent. Omega-equation attribution ideas enable us to quantify the contributions from different physical mechanisms to the total vertical motion, Krishnamurti (1968a, 1968b), Räisänen (1995). Here, these ideas are applied to the ANOMALIA cases, in order to evaluate the different sources of vertical motion. In particular, the Q-vector form of the Quasi-Geostrophic (QG) omega-equation, Hoskins et al. (1978), with diabatic heating/cooling included, is solved numerically using data from the UK Met-Office Unified model.

QG omega-equation attribution has been employed before, Clough and Davitt (1995), Athanassiadou and Thorpe (1995) assuming zero vertical velocity at the lower boundary. The effects of orographic forcing, that is, upslope/downslope motions are implicit in the lower boundary conditions for omega and are expected to be important over a region of complex topography such as the western Mediterranean. These effects appear in the complementary solution of the omega equation.

The vertical velocity $\hat{w}$ thus obtained from the inversion of the omega-equation, is the sum from different but interrelated mechanisms and can be written as

$$\hat{w} = w_{so} + w_{ma} + w_{mt} \qquad (1)$$

where w_{so} is the contribution from synoptic-scale processes (divergence of the Q-vector field), w_{ma} from diabatic effects (due to ascent in a saturated environment) and w_{mt} from upslope/downslope motion at the lower boundary.

3. RESULTS

The synoptic scale contribution was found to be a significant mechanism particularly in those cases where a well defined frontal system was present. The contribution to the total vertical motion from this mechanism was found to be more important in the middle troposphere.

The contribution due to sloping terrain, proved to be important in areas of significant orography, especially when there is strong cross-mountain flow. Lower boundary effects

* *Corresponding author address:* Maria Athanassiadou, Department. of Meteorology, University of Reading, 2 Earley Gate, Whiteknigths, PO Box 239, Reading RG6 6AU, UK; e-mail: <M.Athanassiadou@reading.ac.uk>

should not be neglected when the omega-equation is employed to study vertical motions in areas characterised by complex terrain. The orographic contribution is maximum near the surface and decreases with height. This is not surprising, considering the nature of the solution. This view though, clearly underestimates the true effects of orography since it does not take into account other aspects of orographic flow i.e., mountain waves.

The contribution from diabatic effects (i.e., the "additional" vertical motion induced due to ascent in a moist environment) proved to be a very significant mechanism particularly in areas of heavy precipitation.

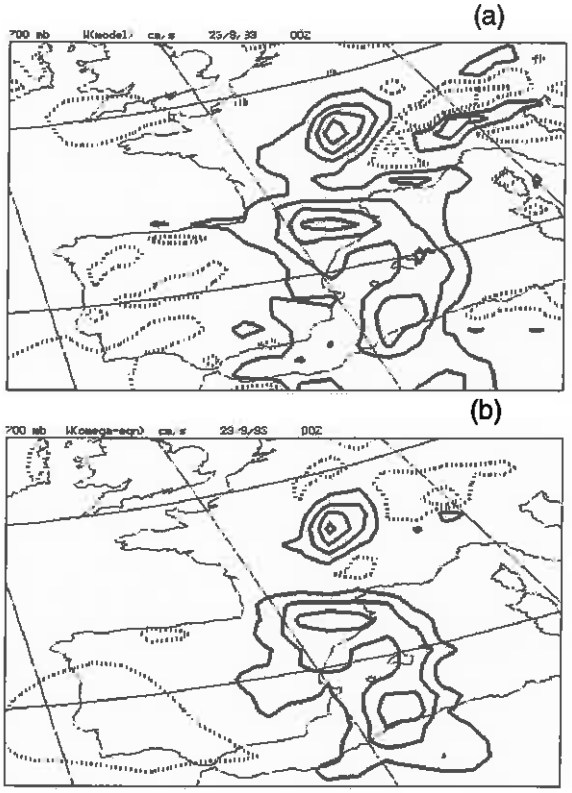

Figure 1. Vertical velocity at 700 mb for 00Z of the 23/9/93. The contour interval is 4 cm/s. First positive contour is 2 cm/s. Positive (negative) values are shown in solid (dashed) contour lines. (a) Analysed (b) From the inversion of the ω-equation

An example is presented here from one of the ANOMALIA cases (Brig). This case is classified of the "synoptic type". It is associated with a low pressure system over S. France and a trough over the Spanish coast. At upper levels a potential vorticity cut-off is found, approaching the area from the West. Fig. 1(a) shows the analysed vertical velocity at 700 *mb* as obtained from the Unified Model. The vertical velocity obtained from the inversion of the omega-equation is shown in Fig. 1(b) for the same pressure level and time.

The patterns of the retrieved vertical velocity resemble the analysed ones very well, both in terms of space distribution and maximum intensity of individual updrafts. The results are very encouraging given the fact that the inversion of the omega-equation is tested over a very complex topography and effects such as gravity waves are excluded from the solution.

The attribution methodology requires careful application but provides the only way to isolate the various forcing mechanisms. For example, the synoptic-scale forcing is often small but nevertheless crucial for the diabatic contribution.

4. ACKNOWLEDGEMENTS

The ANOMALIA project is supported by the EC contract EV5V-CT94-0442.

5. REFERENCES

Athanassiadou M., and A. J. Thorpe 1995,: The ANOMALIA project and MAP. *MAP newsletter*, **no. 3**, 48-50.

Clough S. A. and C.S. A. Davitt, 1995: "Development of an Atlantic frontal wave during IOP 3 of fronts '92" in The Life Cycles of Extratropical Cyclones, **II**, 151-156, *International Symposium 27/6-1/7 94*, Bergen, Norway.

Hoskins B. J., I. Draghici and H. C. Davies, 1978: "A new look at the omega-equation". *Quart. J. R. Meteor. Soc.*, **104**, 31-38.

Krishnamurti T. N., 1968a: "A diagnostic balance model for studies of weather systems of low and high latitudes, Rossby number less than 1", *Mon. Wea. Rev.*, **Vol. 96, No 4**, 197-207

Krishnamurti T. N., 1968b: "A study of a developing wave cyclone", *Mon. Wea. Rev.*, **Vol. 96, No 4**, 208-217

Räisänen J., 1995: "Factors affecting synoptic-scale vertical motions: A statistical study using a generalised omega equation", *Mon. Wea. Rev.*, **Vol. 123**, 2447-2460

P12.8 SINGULAR VECTOR CALCULATIONS FOR CASES OF CYCLOGENESIS IN THE NORTH ATLANTIC STORM–TRACK

Andrea Montani[1,*], Roberto Buizza[2] and Alan J. Thorpe[1]

[1]Joint Centre for Mesoscale Meteorology, University of Reading, UK
[2]European Centre for Medium–Range Weather Forecasts, Reading, UK

1. INTRODUCTION

In particular meteorological situations, most forecast errors are due to a lack of observations used to construct the initial conditions for the forecast model. This is particularly true in oceanic storm–tracks, where the data coverage is poor. These analysis errors, as for other types of small perturbation, have been shown to grow in relatively small "sensitive" regions whose location depends strongly on features of the flow and can vary day by day. One way to (partially) solve this problem consists of performing targeted observations in these sensitive areas in order to reduce as much as possible the analysis errors which will eventually grow.

The Fronts and Atlantic Storm Track EXperiment (FASTEX) aims to perform targeted observations to focus on the generation of storms towards the eastern end of the Atlantic storm–track. Besides studying frontal cyclones in their mature phase, an important part of this experiment (scheduled for January and February 1997) consists of upstream observations, taken by aircraft in mid–Atlantic, the aim of which is to improve the predictability of these systems. In order to improve forecasts, FASTEX will take targeted observations in those areas where analysis errors are likely to be large, to grow rapidly and where the atmosphere is found to be more sensitive to initial errors.

Then, it is necessary to find a technique which makes targeting as effective as possible; this will enable us to know how to "target" our observations, by selecting and exploring only the most sensitive regions of the atmosphere. Singular vectors (SVs) can be used for this purpose. In fact, SVs identify the perturbations characterised by the maximum growth of a predefined quantity (e.g. total energy) during a so called optimisation time interval (OTI, say 48 hours) over a localised area (say, the eastern end of the Atlantic storm–track).

Rabier et al. (1996), for example, proved that SVs can be used to find those areas in which analysis errors, if they exist, will grow rapidly and limit predictability. In fact, SVs are able to describe the growing part of analysis errors, as reported in Buizza et al. (1996). The description of the basic formalism and characteristics of SVs can be found, for example, in Buizza and Palmer (1995). Here, we intend to explore the possibility of a link between SVs and the growth of analysis errors in limited regions. The idea is to use the information given by the SVs at initial time T0 in order to detect those regions where hypothetical extra–observations might be taken.

In preparation for FASTEX, we performed the calculation of localised SVs during winter 1995/96 using the European Centre for Medium–Range Weather Forecasts (ECMWF) forecasting model.

Results of case studies obtained of January and March 1996 are presented with special focus on the structure and evolution of the SVs. Implications for the upstream observations to be taken during FASTEX are made; in particular, special emphasis is given to the location of the sensitive regions 48 hours prior to the intensive observations of the cyclone.

2. CASE–STUDIES

At ECMWF, daily computation of SVs is performed in the following set–up: 48h OTI, spectral triangular truncation T42, 19 vertical levels (T42L19), total energy norm. Moreover, SVs are constructed to be localised, at optimisation time, in the Northern Hemisphere extra-tropics.

In our experiments, the resolution is increased to T63L19 and a target area is defined, in order to investigate those SVs which, at final time, will maximise the energy in the FASTEX mesoscale observing area in the eastern Atlantic. Only a reduced number of SVs are calculated (up to 5) both to save computer time and also because only these vectors are supposed to be responsible for significant growth in such a small target area.

Four cases of January–March 1996, all characterised by secondary cyclone growth, have been studied.

Here one case study is presented, for the system developing between 12Z of 6th January 1996 and 12Z of 8th January 1996. The target area

* *Corresponding author address*: Mr. Andrea Montani, Department of Meteorology, University of Reading, Reading RG6 6AU, UK; e–mail <swrmonta@reading.ac.uk>.

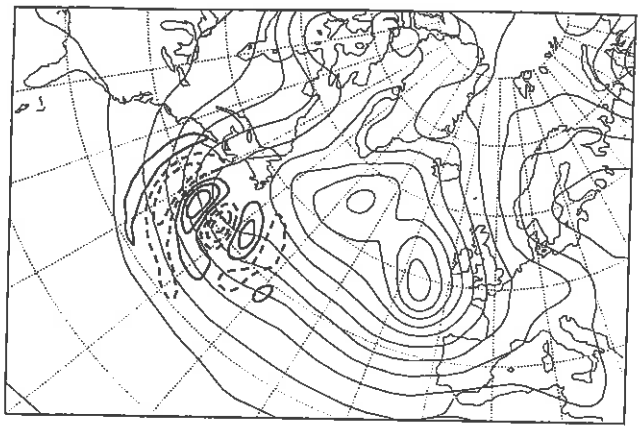

Figure 1: 850 mb geopotential height (contour interval 60 m) and SV=1, plotted in terms of vorticity (contour interval $4{\cdot}10^{-7}s^{-1}$, maximum $1.2{\cdot}10^{-6}s^{-1}$) at model level 15, at 12Z of 6th January 1996.

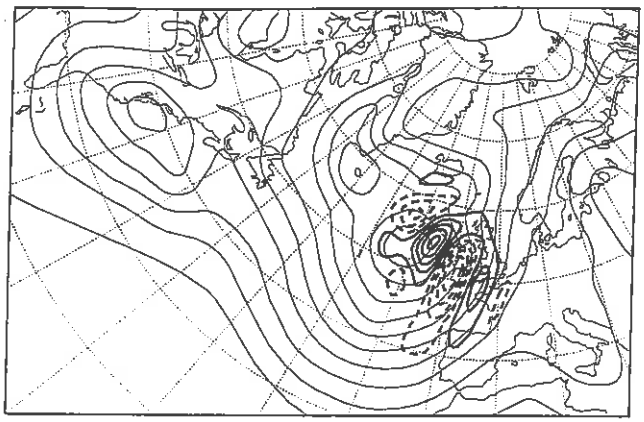

Figure 2: As Figure 1 but at 12Z of 8th January 1996 and with vorticity contour interval of $4{\cdot}10^{-6}s^{-1}$ (maximum $2{\cdot}10^{-5}s^{-1}$).

for this experiment extends between 30N and 80N in latitude, 30W and 10E in longitude. Figure 1 shows, at initial time T0, the most unstable SV superimposed to the atmospheric flow. The SV presents a maximum in vorticity amplification where a small low–tropospheric trough is located. This region is suggested to be the most suitable for extra–observations to be taken. In the following 48 hours, the trough develops into a main cyclone, which becomes the dominant feature in the east end of the Atlantic. At 12Z of 8th January 1996, the system and the SV have evolved as indicated in Figure 2. Peaks in SV structure seem to have followed the system, being located, now, downstream of the pressure minimum.

The SV profile of total energy (Figure 3) shows that there is an initial peak (dashed line) at model level 14, that is around 780 mb. On the contrary, at final time (solid line), a double peak structure is evident, with two maxima located at model level 15 and near the tropopause. It is interesting to speculate about whether it is a coincidence that

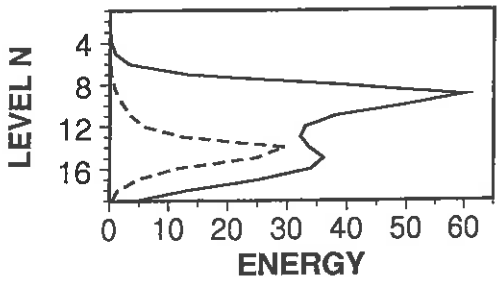

Figure 3: Vertical profile of total energy (in m^2/s^2) at initial (dashed line, ×100) and final time (solid line) for SV=1.

these two zones are known to be typical heights of significant potential vorticity anomalies. The vertical profile at T0 indicates that additional observations should be made in the lower troposphere. It is interesting to compare this finding with the results of mesoscale dynamics studies which indicate that zones of instability may occur both near the tropopause and near the surface.

The possibility of associating peaks in SV plots at T0 with sharp pressure gradients or kinks on elongated fronts has been investigated. These may be associated with incipient frontal cyclones.

3. CONCLUDING REMARKS

It is suggested that SVs could be used to target observations during episodes of secondary cyclone growth in the Atlantic storm–track. Preliminary results for one case study have been discussed in some details. Average results suggest that SVs can be used to detect the most sensitive areas of the atmosphere. When computed with a small final time target region, the first and the second SV offer a good description of location and structure of the fastest growing perturbations. Considered at initial time T0, these SVs indicate a reasonable small target area (about 1000 km wide and preferably located in the west end of the Atlantic) in which to perform upstream observations of incipient cyclones. One of the most controversial results of this study, to be validated during FASTEX campaign, is the suggestion that targeted observations should be performed in the lower troposphere.

4. REFERENCES

Buizza, R., Palmer, T.N., 1995: The singular-vector structure of the atmospheric global circulation. *J. Atmos. Sci.*, **52**, 1434–1456.

Buizza, R., Gelaro, R., Molteni, F., Palmer, T.N., 1996: The impact of increasing resolution in predictability studies with singular vectors. *Quart. J. Roy. Meteor. Soc.*, under revision.

Rabier, F., Klinkler, E., Courtier, P., Hollingsworth, A., 1996: Sensitivity of forecast errors to initial conditions. *Quart. J. Roy. Meteor. Soc.*, **122**, 121–150.

P12.12 A NEW PV-BASED METHOD FOR SHORT-RANGE WEATHER FORECASTING QUALITY CONTROL AND INTERVENTION

Meral Demirtas* and Alan J. Thorpe

Department of Meteorology
University of Reading, UK

1. INTRODUCTION

This paper describes the use of potential vorticity (hereafter PV) in short-range weather forecasting to monitor forecast quality control, and to assess the impact of local PV modifications on the forecast accuracy.

The advantages of PV thinking come from two properties of the PV which are its conservation and its invertibility (Hoskins et al. 1985). The conservation property enables one to identify and follow features in space and time. The invertibility property helps one to quantify the importance of features in terms of, the strength of their associated circulations and their capacity to enhance the development of other features (Davis and Emanuel 1991). [1 PV unit $=10^{-6}m^2s^{-1}Kkg^{-1}$ or 1PVU in short.]

The dynamically most meaningful information can be illustrated on a single chart by using PV on isentropic charts such as 315K or single PV charts such as PV=2. These charts provide compact information and increase understanding of a given forecast. There is a need to check the short-range forecast of PV with latest observations. The Meteosat water vapour (hereafter WV) image is a good tool for this purpose. Dry regions on the image correspond with stratospheric air and high PV, and moist regions correspond with the upper/mid tropospheric air and low PV. Mismatches between the predicted PV on the 315K surface and the WV image give the first indications of a possible forecast problem. If this occurs, one should be able to fit the PV with the WV image. The inversion of this new PV will provide wind and temperature fields. The forecast in question can be re-run by adding in these new extra data. It is the hypothesis here that this new forecast will be more accurate.

* *Corresponding author address:* Ms Meral Demirtas, Univ. of Reading, Dept. of Meteorology, 2 Earley Gate, Reading, RG6 6AU, United Kingdom
E-mail: <swrdemas@reading.ac.uk>

2. A NEW METHOD FOR FORECAST QUALITY CONTROL AND INTERVENTION:

The aim is to explore the existence and nature of key features of the WV image and the PV signatures of mid-latitude cyclones. Light can be shed on how observations and dynamical concepts could be used together to improve our ability to forecast mid-latitude weather systems.

This method draws attention to two main features on satellite imagery and PV charts that could have applications in forecasting. 1. The "cloud head" which is observed prior to a cyclonic development. 2. The "dry intrusion" seen as a "dark region" or so-called "dry slot" on the water vapour imagery.

2.1 Water Vapour Imagery:

Water vapour imagery (WV) is derived from the radiation emitted by water vapour. Most of the radiation reaching a satellite is emitted by WV or cloud in the upper or middle troposphere and is given here by light shades in contrast to dry regions which are black. A satellite typically "sees" moisture or cloud in the layer between 700 mb and 200 mb.

2.2 A Compact Display Form of Atmospheric Dynamics: PV Charts

PV is generally displayed one of the three ways, as PV on an isentropic surface, theta on a constant PV surface or as the height of the PV=2 surface.

In this study the 315K surface for winter, the 330K for summer are used. These surfaces lie over the 300mb levels at high latitudes then intersects with the tropopause at mid-latitudes, and slopes down to the 800 mb levels at low latitudes.

Another chart is the height of the dynamical tropopause or the so-called "PV=2 surface". When the PV=2 height is very low, this means that the tropopause is close to the surface and is bringing high PV values low altitudes. In this kind of situation, it has been observed that surface pressure decreases remarkably.

2.3 Relationships Between the WV Image and PV:

In this work, the above mentioned PV charts were superimposed over the Meteosat WV image. It was noted that high PV values on the 315K surface (or low PV=2 surface heights) generally correspond well with the dark regions on the WV image, while low PV values (or high PV=2 surface heights) match with the bright regions of the WV image.

There is a close relationship between the dry regions on the WV image and the high PV values at the rear of a developing cyclone (Young et al. 1987). Many case studies of cyclogenesis have focused on the role of these PV rich 'dry intrusions' (or sometimes referred to as dry-slots on the WV imagery). It was suggested that these PV anomalies could be responsible major surface developments.

Other important features on the WV image are so-called "cloud heads", known to accompany some explosive cyclogenesis (McCallum and Norris 1990, and Bader et al. 1995).

2.4 Validation and Intervention of a Forecast:

Forecast quality controls can be made by comparing significant WV features with PV charts. Mismatches between them will indicate an error before this is apparent by other means. The next step is to modify PV in these regions and then inverting the new PV to get related wind and temperature fields. These dynamically consistent new data then can be used to re-run the forecast in question.

3. A CASE STUDY BASED ON TESTING THE NEW METHOD:

3.1 Synoptic Overview of 16 February 1995 Storm:

A small wave, situated near 40-45°N 35-45° W by 12 UTC on the 15th, became more pronounced later on. The associated low had the central pressure of 999mb at 06 UTC on the 16th. When the system arrived over western part of the UK, the central pressure was 983 mb at 18 UTC. The associated weather observed over the UK on the 16th February 1995 can be summarised as follows: "Rain, heavy at times, quickly followed in the south-west, spreading to most of England and Wales by evening. With the rain, there were strong, gusty winds, reaching gale force in places. The cloud and rain cleared from all but parts of north-east England during evening, to leave the bulk of England and Wales with clear periods and showers. Scotland and Northern Ireland remained showery, turning wintry over hills. Temperatures were generally mild. Most rain (in 24 hrs from 0900 GMT) was 24.7 mm. [Daily Weather Summary, The Met. Office London Weather Center, 16/02/95]

Inspection of hand driven surface charts showed that from 18 UTC on the 15th to 18 UTC on the 16th, the central pressure of the low decreased from 1007 mb to 983 mb. This means that pressure loss was $1 mbhr^{-1}$ in 24 hours which could be considered as a threshold bomb event.

3.2 Quality Control of the Forecast:

The Meteosat WV image was compared with the PV of the 315K surface at the start of the forecast. It was noted that the PV distributions over the moist regions (indicated by very light shades) do not capture well the developing cloud head shape which was situated at the 48-52° N 25-15° W at 00 UTC. (See figure 1.) Another missing relation was that the tight PV gradient of the tropopause was not over the region of the sharp transition zone of dry and moist air on the image. Although the position of stratospheric high PV (6 PVU), near 52°N 30°W, was situated slightly north of the main dry region (48-50°N 30°W), there was not a very large mismatch.

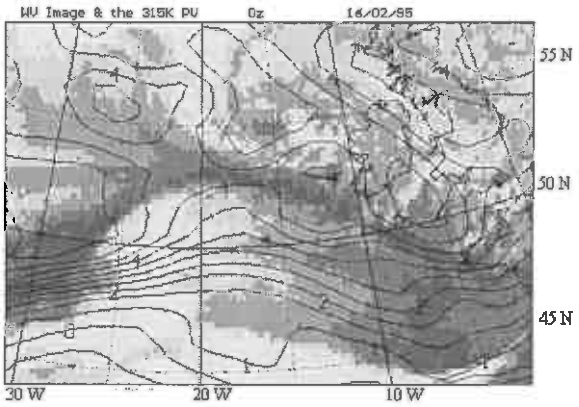

Figure 1: The Meteosat water vapour imagery in grey shades and the 315K surface PV in contours at the start of the forecast 00 UTC on the 16/02/95. Dark shades represent dry air, light shades represent moist air. PV contoured every 0.5 PVU.

This forecast did not get the location and intensity of the system. It also missed most of the rain over mid and northern parts of the UK.

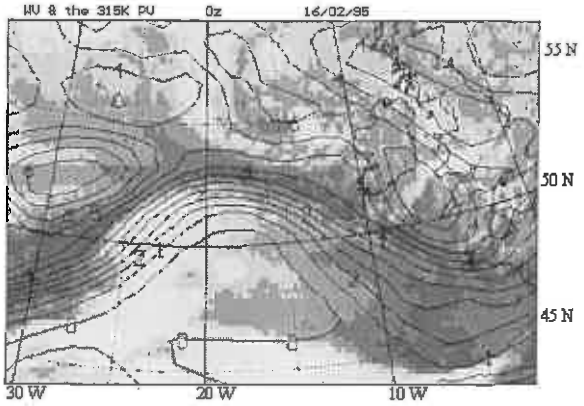

Figure 2: The Meteosat water vapour imagery in grey shades and the 315K surface PV in contours at the start of the re-run 00 UTC on the 16/02/95. Dark shades represent dry air, bright shades represent moist air. PV contoured every 0.5 PVU.

3.3 Performance of the Re-Run Forecast:

Local PV modifications were made over the mismatched region described in the previous section. The new PV was superimposed over the WV image at the start of the forecast. As can be seen from the figure 2, dynamically significant features matched with the image better than the forecast in question.

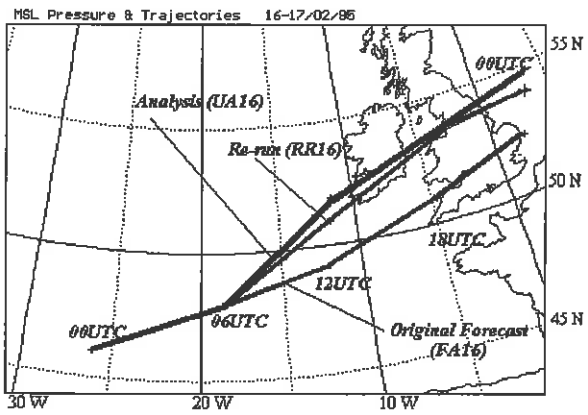

	00UTC	06UTC	12UTC	18UTC	00UTC
UA16	1005.2	1004.2	993.3	987.4	981.5
RR16	1005.3	1002.6	997.0	989.0	984.0
FA16	1005.2	1003.7	999.3	994.5	990.0

Figure 3: MSL pressure centres of the analysis, the re-run and the original forecast shown in dark lines from 00 UTC on the 16th to 00 UTC on the 17th. Locations of the low are indicated by crosses every 6 hours. Related pressure minimum in millibars are tabulated.

The re-run forecast, using the additional data derived from the new PV distribution, predicted the location and intensity of the surface development noticeably better than the original forecast. Figure 3 shows performance of this re-run and the forecast in question.

Radar images were also compared with the analysis, the original forecast and the re-run. (Not shown in here.) It was noted that the re-run captured main rainfall regions.

4. CONCLUSIONS:

A new method, aimed to help forecasters in defining model quality control and provide dynamically consistent data to re-run a potentially poor forecast , was introduced.

The case study shows how the forecast model responded to the application of our new methodology. A much improved forecast was obtained by introducing bogus data suggested by the potential vorticity distributions. This, and other similar cases, give considerable encouragement that potential vorticity concept, can give improvements in short-range weather forecasting.

5. ACKNOWLEDGEMENT:

The authors are grateful to Julian Heming who kindly made the UK Met. Office UM re-runs. The first author would like thank the Turkish Government for the sponsorship.

6. REFERENCES

Bader, M. J., Forbes, G.S., Grant, J. R., Lilley, R. B. E., and Waters, A. J. 1995: Images in the weather forecasting. A practical guide for interpreting satellite and radar imagery. *Cambridge University Press.*

Davis, C. A. and Emanuel, K. A. 1991: Potential vorticity diagnostics of cyclogenesis. *Mon. Wea. Rev.*, **119**, 1929-1953.

Hoskins, B. J., McIntyre, M. E., and Robertson, A. W. 1985: On the use of and significance of isentropic potential vorticity maps. *Q. J. R. Meteor. Soc.*, **111**, 877-946

McCallum, E. and Norris, W. J. T. 1990: The storms of January and February 1990, *Meteorological Magazine*, **119**, 201-210.

Young, M. V., Monk, G. A. and Browning, K. A. 1987: Interpretation of satellite imagery of a rapidly deepening cyclone. *Q. J. R. Meteor. Soc.*, **113**, 1089-1113.

USE OF COINCIDENT AIRCRAFT AND RADAR OBSERVATIONS TO VERIFY AND DERIVE PARAMETERISATION OF CLOUD MICROPHYSICS IN MESOSCALE MODEL FORECAST OF FRONTAL CLOUD

Anthony J Illingworth, Susan P Ballard*, John W G Thomason'
and Virginie Marecal"

Joint Centre for Mesoscale Meteorology, U of Reading, Reading, UK
Present affiliations:
(*) NWP Division UK Meteorological Office, Bracknell, UK
(') University of Newcastle, Newcastle, UK
(") CETP, Issy-les-Moulineaux, France.

1. INTRODUCTION

As more realistic cloud microphysical parameterisation schemes are introduced into operational forecasting models, it becomes more important to validate the various representations by comparing model output with radar and aircraft observations. We investigate a cloud scheme used by Golding (1993) which is a simplification of the Rutledge and Hobbs (1983) and Cox (1988) parameterisations. The scheme allows for separate prediction of cloud liquid water and ice phases as opposed to the temperature dependent parameterisations of cloud phase used previously However, the ice phase is still treated by a combined ice/snow variable which avoids the need for an explicit parameterisation of aggregation. The processes included are: fall of ice/snow; ice/snow nucleation; deposition and sublimation of ice/snow; riming of snow; evaporation of melting snow; melting of snow; evaporation of rain; accretion of cloud water to rain and autoconversion of cloud water to rain.

The size spectra of the ice precipitation are assumed to be an exponential function of size D,

$$N(D) = N_o \exp(-\lambda D). \qquad (1)$$

The value of N_o is often taken as a constant (e.g. Rutledge and Hobbs 1983) but Golding (1993) assumed (after Cox, 1988) a temperature dependence to simulate aggregation. In this study aircraft observations are used to investigate the variability of N_o and λ, and the effect of modifying the model schemes to reflect these spectral changes.

Corresponding author: A.J.Illingworth, Dept of Meteorology, U of Reading, Reading RG6 2AU, UK

We present observations of three frontal passages over Southern England on 21 June 1990, 9 Nov 1993 and 19 October 1994, using data from the UK operational radar network, high resolution polarisation data from the Chilbolton research radar which provided vertical sections of reflectivity and information on hydrometeor type, and in-situ microphysical measurements made by the C-130 aircraft of the UK Met. Office. The data were compared with models which forecast over the UK at about 15km resolution ; the 1990 case study used the non-hydrostatic Golding (1993) model, whereas for 1993 a more recent hydrostatic model was used.

2. AIRCRAFT OBSERVATIONS.

On each day a series of 70km long flight legs was made through the stratiform ice precipitation. Analysis of the ice particle images revealed that they were predominantly aggregates and that for particles above 0.6mm diameter, their size spectra were of the exponential form of Equation (1). The values of N_o and λ were well correlated as revealed in Figure 1, where each value of N_o and λ is derived from ten seconds (1km) of 2D probe data. The straight line fit, covering five orders of magnitude of N_o, is given by

$$N_o = 10^5 \lambda^3 \qquad (2)$$

where N_o is in m^{-4} and λ in mm^{-1}. This dependence was predicted theoretically for aggregating ice particles by Passerelli (1977). Particles <0.6mm size also had exponential spectra but the values of N_o and λ showed much less variation and were not correlated. Ryan's survey (1996) suggests a temperature dependence of λ, but these measurements, covering a 15°C temperature range, find λ better correlated with N_o.

7th AMS Conf on Mesoscale Processes
Reading, UK. September 1996

3. RADAR OBSERVATIONS.

RHI radar scans were made every few minutes on the azimuth along which the aircraft was flying. A typical radar section is shown in Figure 2, which reveals a radar bight band at a height of 2km on 21 June 1990. This bright band was coincident with a high level of cross polar return (LDR > -18dB), confirming that the melting ice particles were low density oblate aggregates. At no time were higher density graupel particles in evidence on these three days. A comparison of the radar reflectivity with the 2D-probe data suggests that the ice water content (IWC in gm^{-3}) is related to the radar reflectivity by:

$$IWC = 0.034\ Z^{0.4} \qquad (3).$$

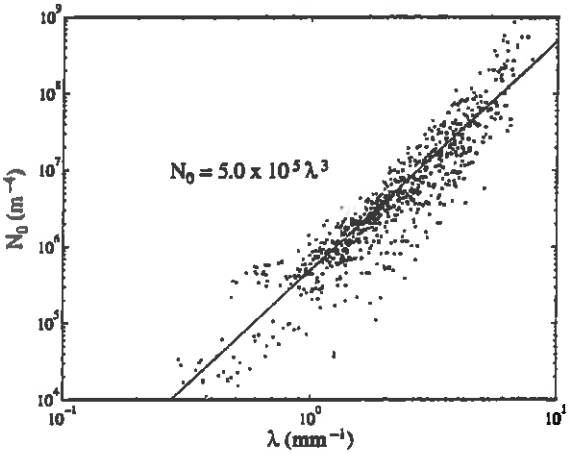

Fig 1. N_o-λspectra for all three flights

Consequently, values of Z of 12, 20 and 24dBZ above the bright band in Figure 2, correspond to values of IWC of 0.1,0.2 and 0.3 gm^{-3} respectively. These values are typical of those recorded on these three days, in that IWC values in stratiform precipitation containing aggregates (snowflakes) do not exceed $0.3gm^{-3}$.

4. MODELLING STUDIES

Figure 3a shows the values of precipitation water content predicted using the Golding 1993 scheme initialised at midnight for 1100h on 21 June 1990 along the same Chilbolton radial as in figure 2. The ice water content values in Figure 3a are over 1 gm^{-3}, much higher than those inferred from the radar.

The cloud scheme was modified to take into account the correlation between N_o and λ^3. The conversion rates between water categories were modified assuming ice mass proportional to D^3 and using the terminal velocity-diameter relationship of Magono and Nakamaura (1965), $V(D)=2.78\ (\rho_i D)^{0.5}$ where ρ_i is ice density and D is in mm, for a constant value of ice density of $0.1gcm^{-3}$. Figure 3b is the corresponding cross section to 3a and shows that the values of IWC are now in closer agreement with the radar observations. However, the liquid water content (LWC) measured by the aircraft were below $0.1gm^{-3}$, whilst the LWC accompanying figure 3b were rather higher than this, with those for 3a being more realistic.

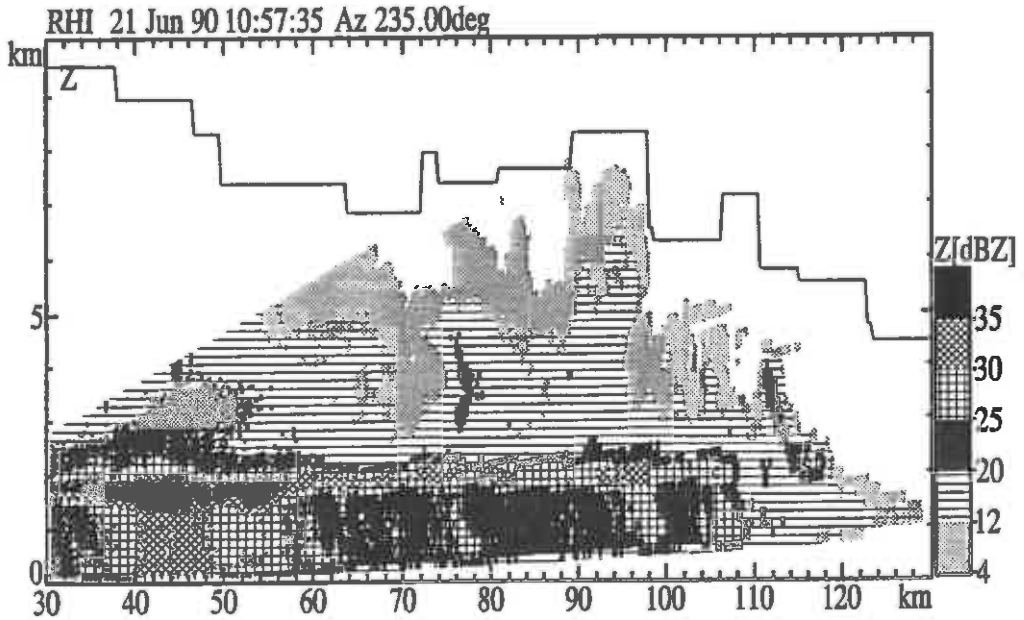

Fig 2. RHI of radar reflectivity for 21 June 91.

Golding (1993), following Cox (1988), assumes mass proportional to D^2 and derived a velocity diameter relationship to fit the widely used Heymsfield (1977) terminal velocity relationship

$$V = 1.089\ IWC^{0.16} \quad (4)$$

Integrating the Magono and Nakamura expression over the N_o - λ^3 size spectra yields:

$$V = 4.26\ IWC^{0.5} \quad (5)$$

and V is independent of ρ_i, provided the ice density does not vary with size. The terminal velocities for equation 5 are much higher for IWC > 0.1gm^{-3} than those for equation 4.

The radar observations for 9 November were compared with the output for the more recent hydrostatic model. In this case at -3.8°C IWC values were about 0.28gm^{-3} whereas radar values were up to 0.2gm^{-3}, but when the changes implied by the N_o - λ relationship were included, the IWC was reduced to a value of about 0.15gm^{-3}. Values of supercooled LWC which were about 0.05gm^{-3} were increased to 0.1gm^{-3} for the modified scheme.

5. DISCUSSION

The various model versions had impacts on the values of ice and liquid water content, but the precipitation rates on the ground were almost unaffected and agreed with those inferred from radar. For the 1990 case the impact of the N_o-λ^3 parameterisation reduced the model IWC by up to a factor of four so that it agreed with the radar inferred IWC, but LWC values were increased slightly. The impact in the 1993 case was similar in that IWC was reduced and supercooled LWC increased but the benefit less clear cut.

More investigation is needed to understand the effect on LWC, but it seems that at high IWC the low N_o does not correctly simulate the observed concentration of ice particles with size < 0.6mm, which may be important in converting liquid water to ice. However, it is clear that the higher terminal velocities predicted using N_o - λ^3 at higher values of IWC are responsible for preventing excessive IWC values.

6. ACKNOWLEDGEMENTS

We would like to thank colleagues at RAL (RCRU) for the Chilbolton radar data and those at the Meteorological Research Flight for supplying the aircraft data. The work was partly supported by NERC grant GST/02/718.

7. REFERENCES.

Cox, G.P., 1988: Modelling precipitation in frontal rainbands. Quart J Roy Meteorol Soc, **114**, 115-127.

Golding,B.W., 1993: A numerical investigation of tropical island thunderstorms. Mon Wea Rev, **121**, 1417-1433.

Heymsfield A.J., 1977: Precipitation development in stratiform ice clouds: a microphysical and dynamical study. J.Atmos.Sci, **34**, 367-381.

Magono,C. & Nakamaura,T., 1965: Aerodynamics of fallings snowflakes J Met Soc Japan, **43**, 139-147.

Passarelli R.E., 1978: An approximate analytical model of the vapour deposition and aggregation growth of snowflakes. J.Atmos. Sci., **35**, 118-124.

Rutlege, S.A and Hobbs, P.V., 1983: The mesoscale and microscale structure and organization of clouds and precipitation in mid-latitude cyclones. Part VII: A model for the "seeder-feeder" process in warm-frontal rainbands. J.Atmos.Sci, **40**,1185-1206.

Ryan,B.F., 1966: On the global variation of precipitating layer clouds. Bull Amer Meteorol Soc, **77**, 53-70.

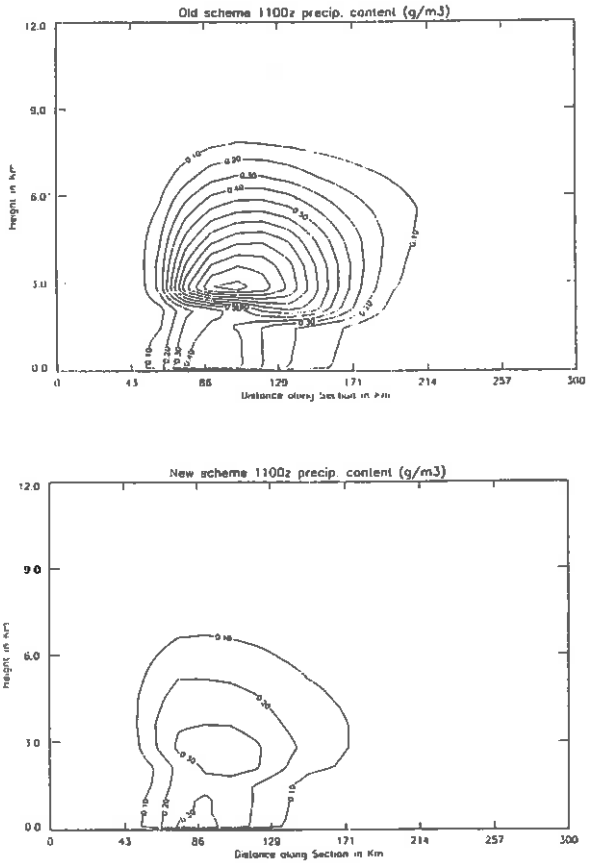

Fig 3. Predicted values of precipitation water content for a) Golding (1993) scheme (upper) and b) the modified scheme (lower panel).

CURRENT JCMM INTERNAL REPORTS

This series of JCMM Internal Reports, initiated in 1993, contains unpublished reports and also versions of articles submitted for publication. The complete set of Internal Reports is available from the National Meteorology Library on loan, if required.

1. **Research Strategy and Programme.**
   K A Browning et al
   January 1993

2. **The GEWEX Cloud System Study (GCSS).**
   GEWEX Cloud System Science Team
   January 1993

3. **Evolution of a mesoscale upper tropospheric vorticity maximum and comma cloud from a cloud-free two-dimensional potential vorticity anomaly.**
   K A Browning
   January 1993

4. **The Global Energy and Water Cycle**
   K A Browning
   July 1993

5. **Structure of a midlatitude cyclone before occlusion.**
   K A Browning and N Roberts
   July 1993

6. **Developments in Systems and Tools for Weather Forecasting.**
   K A Browning and G Szejwach
   July 1993

7. **Diagnostic study of a narrow cold frontal rainband and severe winds associated with a stratospheric intrusion.**
   K A Browning and R Reynolds
   August 1993

8. **Survey of perceived priority issues in the parametrizations of cloud-related processes in GCMs.**
   K A Browning
   September 1993

9. **The Effect of Rain on Longwave Radiation.**
   I Dharssi
   September 1993

10. **Cloud Microphysical Processes - A Description of the Parametrization used in the Large Eddy Model.**
H Swann
July 1994

11. **An Appreciation of the Meteorological Research of Ernst Kleinschmidt.**
A J Thorpe
May 1992

12. **Potential Vorticity of Flow Along the Alps.**
A J Thorpe, H Volkert and Dietrich Heimann
August 1992

13. **The Representation of Fronts.**
A J Thorpe
January 1993

14. **A Parametrization Scheme for Symmetric Instability: Tests for an Idealised Flow.**
C S Chan and A J Thorpe
February 1993

15. **The Fronts 92 Experiment: a Quicklook Atlas.**
Edited by T D Hewson
November 1993

16. **Frontal wave stability during moist deformation frontogenesis. Part 1. Linear wave dynamics**
C H Bishop and A J Thorpe
May 1993

17. **Frontal wave stability during moist deformation frontogenesis. Part 2. The suppression of non-linear wave development.**
C H Bishop and A J Thorpe
May 1993

18. **Gravity waves in sheared ducts.**
S Monserrat and A J Thorpe
October 1993

19. **Potential Vorticity and the Electrostatics Analogy: Quasi-Geostrophic Theory.**
C Bishop and A J Thorpe
November 1993

20. **Recent Advances in the Measurement of Precipitation by Radar.**
A J Illingworth
April 1993

21. **Micro-Physique et Givrage. Cloud Microphysics and Aircraft Icing.**
A J Illingworth
May 1993

22. **Differential Phase Measurements of Precipitation.**
M Blackman and A J Illingworth
May 1993

23. **Estimation of Effective Radius of Cloud Particles from the Radar Reflectivity.**
N I Fox and A J Illingworth
May 1993

24. **A Simple Method of Dopplerising a Pulsed Magnetron Radar.**
L Hua, A J Illingworth and J Eastment
November 1993

25. **Radiation and Polar Lows.**
George C Craig
February 1994

26. **Collected preprints submitted to International Symposium on the Life Cycles of Extratropical Cyclones; Bergen, Norway, 27 June - 1 July 1994**
April 1994

27. **Convective Frontogenesis**
Douglas J Parker and Alan J Thorpe
April 1994

28. **Improved Measurement Of The Ice Water Content In Cirrus Using A Total Water Evaporator**
Philip R A Brown and Peter N Francis
April 1994

29. **Mesoscale Effects of a Dry Intrusion within a Vigorous Cyclone**
K A Browning and B W Golding
April 1994

30. **GEWEX Cloud System Study, Science Plan**
May 1994

31. **Parametrization of Momentum Transport by Convectively Generated Gravity Waves**
R Kershaw
February 1995

32. **Mesoscale Modelling Newsletter, No. 5**
May 1994

33. **Observations of the mesoscale sub-structure in the cold air of a developing frontal cyclone**
K A Browning, S A Clough, C S A Davitt, N M Roberts and T D Hewson
May 1994

34. **Longwave Radiative Forcing of a Simulated Tropical Squall Line**
Imtiaz Dharssi
July 1994

35. **On the nature of the convective circulations at a kata-cold front**
K A Browning
September 1994

36. **Collected preprints of papers submitted to the COST-75 International Seminar on Advanced Weather Radar Systems, Brussels, 20-23 September 1994**
November 1994

37. **Use of satellite imagery to diagnose events leading to frontal thunderstorms: Parts I and II of a case study**
K A Browning and N M Roberts
November 1994

38. **The role of spaceborne millimetre-wave radar in the global monitoring of ice cloud**
P R A Brown, A J Illingworth, A J Heymsfield, G M McFarquhar, K A Browning and M Gosset
December 1994

39. **Potential Vorticity Inversion**
Michal Ziemianski
October 1994

40. **Theory of mature tropical cyclones; A comparison between Kleinschmidt (1951) and Emanual (1986)**
Suzanne L Gray
December 1994

41. **Dispersion and removal of pollutants during the passage of an atmospheric frontal system**
N R Gimson
December 1994

42. **The role of snow sublimation in frontogenesis**
D J Parker and A J Thorpe
December 1994

43. **Potential vorticity and the electrostatics Analogy: Ertel-Rossby formulation**
A J Thorpe and C H Bishop
December 1994

44. **Mesoscale aspects of extratropical cyclones: an observational perspective**
K A Browning
January 1995

45. **A Polar Low Outbreak: Evolution and Mesoscale Structures**
T D Hewson, G C Craig and C Claud
February 1995

46. **Generation of near-surface gusts by deep convection**
K Nakamura and R Kershaw
April 1995

47. **Attribution concepts applied to the omega equation**
S A Clough, C S A Davitt and A J Thorpe
June 1995

48 **Parametrization of mixed-phase cloud and precipitation**
Susan P Ballard and M Gerard Hutchinson
June 1995

49 **Short-range forecasting of stratocumulus: Initialization V Prediction**
Susan P Ballard, Simon D Jackson and B Macpherson
June 1995

50 **Contributions of the JCMM/Dept of Meteorology Radar Group to the 27th AMS Radar Meteorology Conference, Vail October 1995**
June 1995

51 **Cold pools in shear**
Douglas J Parker
September 1995

52 **High-resolution analysis of frontal fracture**
K A Browning, S P Ballard and C S A Davitt
September 1995

53 **The Albedo of Broken Cloud Fields: Calculations using a modified two stream radiation code**
Imtiaz Dharssi and Roy Kershaw
October 1995

54 **Parametrization of momentum transport by convection. I: Theory and cloud modelling results**
R Kershaw and D Gregory
November 1995

55 **Variation of frontal structure along a cold front**
K A Browning and N M Roberts
November 1995

56 **Secondary Frontal Waves**
Douglas Parker
December 1995

57 **Objective Fronts**
T D Hewson
March 1996

58 **Mesoscale analysis of the activation of a cold front during cyclogenesis**
K A Browning, N M Roberts and A J Illingworth
June 1996

59 **Investigation of different representations of rain in a 1-d evaporation model**
H Swann
May 1996

60 **Parametrization of diabatic processes in the inversion of the omega-equation**
M Athanassiadou and A J Thorpe

61 **The role of the environmental flow in the development of secondary frontal cyclones**
I A Renfrew, A J Thorpe and C H Bishop

62 **Consequences of the geostrophic momentum approximation on barotropic instability**
S Malardel, A J Thorpe and A Joly
June 1996

63 **Contributions to the AMS/RMS Conference on Mesoscale Processes Reading, 9-13 September 1996**
June 1996

Met Office Joint Centre for Mesoscale Meteorology Department of Meteorology
University of Reading PO Box 243 Reading RG6 6BB United Kingdom
Tel: +44 (0)118 931 8425 Fax: +44 (0)118 931 8791
www.metoffice.com